The stellar mass distribution in early-type disc galaxies

Noordermeer, E.; van der Hulst, J. M.

Published in:
Monthly Notices of the Royal Astronomical Society

DOI:
10.1111/j.1365-2966.2007.11532.x

Publication date:
2007

Mon. Not. R. Astron. Soc. **376,** 1480–1512 (2007) doi:10.1111/j.1365-2966.2007.11532.x

The stellar mass distribution in early-type disc galaxies: surface photometry and bulge–disc decompositions

E. Noordermeer[1,2]⋆ and J. M. van der Hulst[1]

[1]*Kapteyn Astronomical Institute, University of Groningen, PO Box 800, 9700 AV Groningen, the Netherlands*
[2]*University of Nottingham, School of Physics and Astronomy, University Park, NG7 2RD Nottingham*

Accepted 2006 December 19. Received 2006 December 18; in original form 2006 September 28

ABSTRACT

We present deep *B*- and *R*-band surface photometry for a sample of 21 early-type disc galaxies with morphological types between S0 and Sab and absolute *B*-band magnitudes between −17 and −22. Six galaxies were also observed in the *I*-band. We present radial profiles of surface brightness, colour, ellipticity, position angle and deviations of axisymmetry for all galaxies, as well as isophotal and effective radii and total magnitudes. We have decomposed the images into contributions from a spheroidal bulge with a general Sérsic profile and a flat disc with an arbitrary intensity distribution, using an interactive, 2D decomposition technique. We caution against the use of simple 1D decomposition methods and show that they can lead to systematic biases, particularly in the derived bulge parameters.

We study in detail the relations between various bulge and disc parameters. In particular, we find that the bulges of our galaxies have surface brightness profiles ranging from exponential to De Vaucouleurs, with the average value of the Sérsic shape parameter n being 2.5. In agreement with previous studies, we find that the shape of the bulge intensity distribution depends on luminosity, with the more luminous bulges having more centrally peaked light profiles (i.e. higher n). By comparing the ellipticity of the isophotes in the bulges to those in the outer, disc-dominated regions, we are able to derive the intrinsic axis ratio $q_{\rm b}$ of the bulges. The average axis ratio is 0.55, with a rms spread of 0.12. None of the bulges in our sample is spherical, whereas in some cases, the bulges can be as flat as $q_{\rm b} = 0.3$–0.4. The bulge flattening seems to be weakly coupled to luminosity, more luminous bulges being on average slightly more flattened than their lower luminosity counterparts. Our finding that most bulges are significantly flattened and have an intensity profile shallower than $R^{1/4}$ suggests that 'pseudo-bulges', formed from disc material by secular processes, do not occur in late-type spiral galaxies only, but are a common feature in early-type disc galaxies as well.

Most galaxies in our sample have radial colour gradients, becoming bluer towards larger radii. Although this can partly be explained by the radially declining contribution of the red bulges to the observed light, we show that discs must also have intrinsic colour gradients.

Key words: galaxies: fundamental parameters – galaxies: kinematics and dynamics – galaxies: photometry – galaxies: spiral – galaxies: stellar content – galaxies: structure.

1 INTRODUCTION

One of the outstanding problems in our understanding of the structure and evolution of galaxies is the role played by dark matter. Paradoxically, however, one of the main obstacles towards an exact measurement of the amount and distribution of dark matter is, in many cases, formed by our limited knowledge of the contribution of the stars to the gravitational potential. The contribution of the stellar component is expected to be particularly important in early-type disc galaxies. Early-type disc galaxies are among the brightest galaxies in the Universe, in terms of both total luminosity and surface brightness (Roberts & Haynes 1994). It is to be expected that in these galaxies, the stellar mass is dynamically much more important than in low-luminosity and low surface brightness (LSB) galaxies, which are generally believed to be dark matter dominated (e.g. Carignan & Freeman 1988; de Blok & McGaugh 1997; Swaters 1999; Côté, Carignan & Freeman 2000).

⋆E-mail: edo.noordermeer@nottingham.ac.uk

Historically, spiral galaxies were considered as a combination of a more or less spherical bulge and a flattened disc. Bulges were normally modelled as miniature elliptical galaxies, with surface brightness following an $R^{1/4}$-law (following de Vaucouleurs 1948, 1958), whereas the azimuthally averaged disc brightness was usually described with an exponential profile (de Vaucouleurs 1959; Freeman 1970).

It was readily noted that not all galactic discs are well described by simple exponential profiles at all radii (Freeman 1970; van der Kruit 1979), and recent developments have shown that many bulges are not the simple, structureless spherical bodies as previously thought either. *Hubble Space Telescope* (*HST*) observations by Carollo et al. (1997) and Carollo, Stiavelli & Mack (1998) of the cores of 75 spiral galaxies revealed a wealth of nuclear structure, including nuclear spirals, rings and dust lanes. Many of their galaxies showed signs of nuclear star formation. Erwin & Sparke (1999, 2002) and Erwin et al. (2003) showed that many galaxies have nuclear bars and other disc-like structures in their centres. They noted that the central light concentrations in many spiral galaxies seem to originate from highly flattened structures, rather than from spherical bodies. The photometric profiles of many spiral galaxy bulges are described better by exponential or $R^{1/2}$-profiles than by the classical $R^{1/4}$-law (Andredakis & Sanders 1994; Andredakis, Peletier & Balcells 1995; Courteau, de Jong & Broeils 1996; de Jong 1996a; Carollo 1999). Finally, spectroscopic observations show that many bulges are much more rotationally supported than elliptical galaxies (Illingworth & Schechter 1982; Kormendy & Illingworth 1982; Kormendy 1993; see also the recent results from the SAURON project for an overview of the complex dynamics, including disc-like rotation, in the centres of many spiral galaxies: Emsellem et al. 2004; Fathi 2004).

All these observations led Kormendy & Kennicutt (2004) to postulate that many central light concentrations are not classical, spheroidal bulges with a similar formation history as ellipticals, but rather disc-like structures, formed by secular processes; they call these disc-like bulges 'pseudo-bulges'.

For a study of the global dynamics of spiral galaxies, a proper understanding of the structure of bulges and discs is crucial. Irrespective of the exact formation mechanism of (pseudo-)bulges, they will have experienced a different evolutionary history than their surrounding discs. As a result, their stellar populations, and corresponding mass-to-light ratios, are expected to be different. Accurate bulge–disc decompositions are therefore needed to determine the contribution of each component to the gravitational potential. Furthermore, the vertical structure of the bulge has a strong influence on the peak rotation velocity in a galaxy: a flat, disc-like structure will generally have a higher circular rotation speed in the plane than a spherical system with the same projected surface density (see e.g. fig. 2–12 in Binney & Tremaine 1987).

The current paper is part of a larger study of the relation between dark and luminous matter in nearby, early-type disc galaxies. In a previous paper (Noordermeer et al. 2005, hereafter Paper I), we presented H I observations of a sample of 68 such galaxies. In an accompanying paper to the current one (Noordermeer et al. 2007), we present rotation curves for a subset of the galaxies from Paper I, and in a future publication, we will compare them to the rotation velocities expected from the visible matter in order to infer the dark matter distribution. Here, we present another ingredient for our study, a study of the dynamical impact of the bulges and discs in our galaxies. We present *B*-, *R*- and *I*-band surface photometry for a subsample of 21 galaxies from Paper I, with morphological type ranging from S0 to Sab and absolute *B*-band magnitudes $-17 > M_B > -22$. We have decomposed the images into contributions of a flattened disc (including rings, bars, etc.) and a spheroidal bulge with a genuine 3D structure, using an interactive 2D decomposition technique. The radial distribution of stars in each component is then carefully measured and luminosity profiles are constructed and fitted with a general Sérsic profile (bulge) and exponential disc.

In addition to their use in the mass models described above, our data also provide interesting information about the internal structure of bulges and their relation with the surrounding discs. We present an analysis on the various correlations between different bulge and disc parameters and briefly discuss the implications for different bulge-formation mechanisms.

The structure of this paper is as follows. We describe the sample selection in Section 2. The observations and data reduction steps are described in Section 3. In Section 4, we discuss the photometric analysis of the galaxies, including the derivation of radial surface brightness profiles, total magnitudes, diameters, etc. In Section 5, the consistency of our photometric results is checked by comparing different observations of the same galaxies. In Section 6, we present the procedure that was developed to decompose our images into bulge and disc contributions. We discuss the implications of our results in Section 7. Finally, the individual galaxies in our sample are discussed in Section 8, and a brief summary of our study and the main conclusions is presented in Section 9. For clarity, all long tables have been placed at the end of the paper (i.e. in Appendix A). In Appendix B, we show the images and photometric profiles for all galaxies and the results from the bulge–disc decompositions.

2 SAMPLE SELECTION

The galaxies studied in this paper form a subset of the 68 galaxies with H I observations from Paper I, which themselves were selected from the Westerbork Survey of H I in Spiral and Irregular Galaxies (WHISP) (Kamphuis, Sijbring & van Albada 1996; van der Hulst, van Albada & Sancisi 2001). The WHISP sample consists of galaxies on the Northern hemisphere ($\delta > 20^\circ$), with optical diameter and H I line flux limits of $D_{25} > 1$ arcmin and $f > 20$ mJy, respectively. The sample of Paper I consisted of all galaxies in the WHISP survey with morphological type between S0 and Sab. A more detailed description of the parent sample and the properties of the selected galaxies is given in Paper I.

Given the context of the present paper as part of our larger study of rotation curves and dark matter in early-type disc galaxies, the selection of galaxies from the parent sample in Paper I was mainly based on the requirement that good rotation curves could be derived. In practice, the following, somewhat subjective criteria were used: (i) the H I velocity field must be well resolved (>5–10 beams across) and defined over significant parts of the discs (i.e. not confined to small 'patches'); (ii) the gas must be moving in regular circular orbits around the centre of the galaxy. Strongly interacting galaxies, strongly barred galaxies or galaxies with otherwise distorted kinematics are excluded; (iii) the inclination angle must be well constrained and preferably lie between 40° and 80°.

Very few galaxies from Paper I satisfy all these conditions and a strict application of these criteria would lead to a very small sample. For the present paper, we have therefore relaxed the selection criteria and included a number of galaxies with e.g. bars, mild kinematical distortions or a more face-on orientation.

Although the sample-selection criteria described above may, at first sight, appear somewhat irrelevant for a study of bulge and disc properties, we believe that our galaxies form a representative sample of early-type disc galaxies. In Paper I, we showed that the galaxies

Table 1. Sample galaxies: basic data. (1) UGC number, (2) alternative name, (3) morphological type (taken from NED[a]), (4) absolute *B*-band magnitude and (5) distance (from Paper I).

UGC	Alternative name	Type	M_B (mag)	D (Mpc)
(1)	(2)	(3)	(4)	(5)
89	NGC 23	SB(s)a	−21.45	62.1
94	NGC 26	SA(rs)ab	−20.32	62.6
624	NGC 338	Sab	−20.83	65.1
1541	NGC 797	SAB(s)a	−21.12	77.0
2487	NGC 1167	SA0-	−21.88	67.4
2916	–	Sab	−21.05	63.5
2953	IC 356	SA(s)ab pec	−21.22	15.1
3205	–	Sab	−20.89	48.7
3546	NGC 2273	SB(r)a	−20.02	27.3
3580	–	SA(s)a pec:	−18.31	19.2
3993	–	S0?	−20.19	61.9
4458	NGC 2599	SAa	−21.38	64.2
5253	NGC 2985	(R')SA(rs)ab	−20.93	21.1
6786	NGC 3900	SA(r)0+	−19.93[b]	25.9
6787	NGC 3898	SA(s)ab	−20.00	18.9
8699	NGC 5289	(R)SABab:	−19.48	36.7
9133	NGC 5533	SA(rs)ab	−21.22	54.3
11670	NGC 7013	SA(r)0/a	−19.20	12.7
11852	–	SBa?	−20.44	80.0
11914	NGC 7217	(R)SA(r)ab	−20.27	14.9
12043	NGC 7286	S0/a	−17.53	15.4

[a]The NASA/IPAC Extragalactic Data Base (NED; http://nedwww.ipac.caltech.edu) is operated by the Jet propulsion Laboratory, California Insitute of Technology, under contract with the National Aeronautics and Space Administration.

[b]No *B*-band data available in this study; M_B taken from The Lyon Extragalactic Data base (LEDA; http://leda.univ-lyon1.fr/).

in the parent sample resemble very much 'average' early-type disc galaxies. The additional selection for the current paper, based on the kinematical properties described above, is unlikely to introduce a bias towards any particular bulge or disc properties.

In total, the current sample consists of 21 galaxies; a few basic characteristics of the members are given in Table 1. The distances in the table were taken from Paper I and were based on the systemic velocities derived there, corrected for Virgo-centric inflow, and a Hubble constant of $75\,\mathrm{km\,s^{-1}\,Mpc^{-1}}$. The majority of the galaxies in our sample are luminous (16 systems have $M_B < -20$). Of the 21 galaxies, 16 are classed as spirals (type Sa or Sab) and three as lenticulars (S0− to S0+); the remaining two fall in the transitional S0/a class.

3 OBSERVATIONS AND DATA REDUCTION

We have obtained images of all our galaxies in Harris *R* and *B* bands, with a few additional observations in Harris *I* band; for UGC 6786, only *R*-band data were available. The bulk of the observations described here were performed during four observing runs in 2000 and 2001 with the 1.0-m Jacobus Kapteyn Telescope (JKT) at the Observatorio Roque de los Muchachos on La Palma.[1] A few observations were performed at the JKT in service mode in 2002. In all cases, we used the JAG-CCD camera which was equipped with a 2048 × 2048 SITe chip with a pixel size of 0.33 arcsec and a total unvignetted field-of-view of approximately 10 × 10 arcmin^2.

A small number of observations were done using the Wide Field Camera on the 2.5-m INT on La Palma. It was equipped with four 4096 × 2048 EEV CCDs with 0.33-arcsec pixels, offering a total field of view of 34 × 34 arcmin^2.

Finally, a few images were taken with the 8-K Imaging Camera at the 2.4-m MDM Hiltner telescope at Kitt Peak, Arizona. It contains a mosaic of eight 4096 × 2048 SITe CCDs with 0.18-arcsec pixels and a total field of view of 24 × 24 arcmin^2.

Typical exposure times for all observations on the JKT were 30–50 min per band, usually broken up into at least two shorter exposures to enable cosmic ray rejection. Sometimes, more but shorter exposures were taken to prevent the bright cores of the images from saturating on the chip. For the observations at the larger INT and MDM telescopes, we used correspondingly shorter exposures to achieve roughly the same sensitivity as with our exposures on the JKT.

During some nights, the observing conditions were non-photometric due to thin cirrus-clouds, and in some other nights the seeing was very poor. Useful images could still be taken on those nights, but in the former case the absolute photometric calibration was not reliable, whereas in the latter case the central light concentrations were poorly resolved. Those problems were fixed by re-observing the galaxies with short exposure times later. A few galaxies were observed in good conditions several times. Those observations are used in Section 5 to check the consistency of our observations. In Table A1, we list the observations of all galaxies.

Data reduction was performed within the IRAF environment.[2] Standard procedures were followed to subtract readout bias and apply flat-field corrections. Separate exposures for each galaxy were aligned using a number of bright stars. They were then combined, using a simple rejection criterion to remove cosmic ray events and cosmetic defects on the chip.

Special care was taken in the subtraction of the background light. In the first three runs on the JKT, the camera suffered from light-leaks which caused faint residual gradients in the background after flat-fielding, especially in the *R*-band images. In almost all cases, the residuals could be removed by fitting a first- or second-order 2D polynomial to the background and subtracting it from the image. In a few cases, we used polynomials up to the order of 5. In all the cases, extreme care was taken to exclude the image of the galaxy from the fitting region, so as not to subtract any light from the galaxy itself.

In all other observations, including the *B*-band observations from the JKT runs with light-leaks, the flat-fielding worked very well and residuals were small. For these images, the background was removed by fitting a first-order polynomial to the emission-free regions.

As an extra check that the light-leaks did not affect our results, we re-observed UGC 2953 and 3546 in the fourth observing run on the JKT, when the light-leaks were eliminated. Comparison of the resulting photometric profiles from the images with and without light-leaks shows that the gradients were adequately removed and that the resulting profiles are consistent within the errors (see Section 5).

[1] The JKT and Isaac Newton Telescope (INT) are operated on the island of La Palma by the Isaac Newton Group in the Spanish Observatorio del Roque de los Muchachos of the Instituto de Astrofisica de Canarias. Part of the data described in this study was collected via the service observation scheme of the Isaac Newton Group.

[2] IRAF is distributed by the National Optical Astronomy Observatories, which are operated by the Association of Universities for Research in Astronomy, Inc., under cooperative agreement with the National Science Foundation.

Throughout the nights, standard star fields from Landolt (1992) were observed at intervals of 1–2 h. Using the instrumental fluxes of the stars and the magnitudes given by Landolt, we fitted the magnitude zero-points and extinction coefficients, such that

$$m_{\rm Landolt} = m_{\rm obs} + m_0 + e\mathcal{A}, \quad (1)$$

where $m_{\rm Landolt}$ is the stellar magnitude given by Landolt, $m_{\rm obs}$ is our instrumental magnitude, m_0 is the magnitude zero-point, e is the extinction coefficient and $\mathcal{A}$ is the airmass. The coefficients were determined for each night and each colour separately. The errors Δm_0 and Δe on the fitted coefficients were used to derive the photometric error for each observation:

$$\sigma_{\rm phot} = \sqrt{\Delta m_0^2 + (\Delta e\ \mathcal{A})^2}. \quad (2)$$

The resulting errors for all observations are given in Table A1. The average photometric errors for our *B*-, *R*- and *I*-band observations are, respectively, 0.13, 0.11 and 0.11 mag, and, respectively, 90, 76 and 83 per cent have $\sigma_{\rm phot} < 0.2$ mag.

Coordinate systems were added to the images by registering a number of bright stars with known coordinates from the Digitized Sky Survey (DSS). Typical rms errors were of the order of 0.15 arcsec for the JKT images and 0.2 arcsec for the larger INT and MDM images. Note, however, that the uncertainty in the coordinate system of the DSS is about 0.6 arcsec (Russell et al. 1990; Véron-Cetty & Véron 1996). Thus, the coordinate systems of our images are effectively limited by the uncertainties in the DSS and have an accuracy of no better than 0.6 arcsec.

Finally, the images were cleaned from foreground stars, background galaxies and any possible artefacts not removed in the previous steps. For the foreground stars, we fitted a 2D analytical point spread function (PSF) to ≈20 bright, unsaturated stars on the image. Subsequently, all point sources in the image were detected, and the flux in each was determined. The PSF was then scaled to the measured flux and model stellar 'images' were subtracted from the image. This proved to work in a satisfactory manner only for relatively faint stars. For bright stars, the analytical PSF often did not represent the stellar images sufficiently well, and significant residuals remained present in the image after subtraction. Saturated stars, background galaxies and other artefacts in the images could, naturally, not be removed with this method either. All these were removed by hand, masking out the affected regions from the image. Special care was taken to remove faint haloes of bright stars. The same masks were used for all images of a galaxy in different bands to ensure that the measured magnitudes and surface brightnesses refer to the same regions.

4 PHOTOMETRIC PROPERTIES

Photometry was performed at concentric elliptical annuli, using the ELLIPS task from the STSDAS ISOPHOTE package (Jedrzejewski 1987). The ellipses were defined at logarithmic intervals in semi-major axis, starting at ≈0.3 arcsec and increasing the radius of each successive ellipse by a factor of 1.1.

4.1 Isophote orientation parameters

The orientation parameters of the ellipses were determined from the *R*-band images in two steps.

First, ellipses were fit to the image with the position of the centre, position angle and ellipticity of each ellipse left as free fitting parameters. From these fits, the central positions of the galaxies were determined. The bulges of most galaxies create a clear central peak in the image and the centres of the inner ellipses converge usually to a narrowly defined value; often the variation between the inner ellipses is smaller than 0.1 arcsec. In these cases, the error in the absolute central position is dominated by the uncertainty in the coordinate system (see Section 3). In a small number of cases, dust obscures the very centre of the image, and the light distribution is more irregular. Since in those cases the brightest pixels lie at the position of least obscuration, rather than at the true centre of the underlying light distribution, the inner isophotes cannot be used to determine the centre and we rather used the ones at intermediate radii where the effect of dust is either smaller or averages out over the ellipse. The central positions of those galaxies are, however, necessarily less accurately determined than for the ones where we can see into the centre directly. The fitted centres are listed in Columns (2) and (3) in Table A2; the uncertainty and its dominant source are given in Columns (4) and (5), respectively.

In the second step, we did fits with the centre of each ellipse fixed at the position just determined, but with ellipticity and position angle still free. The fitted orientation parameters are shown by the symbols in the top right panels in Figure B1. In the outer part of the galaxies, outside the region where bulges and bars complicate the picture, they usually converge to more or less constant values (see UGC 3205, 3580 and 6787 for nice examples). These values were then assumed to represent the true position angle and inclination of the galaxy. In some cases, however, the position angle and/or ellipticity never converge, and either keeps varying till the last point (e.g. UGC 89, 1541 or 4458) or show several plateaus (e.g. UGC 9133). In these cases, we visually compared the fitted isophotes to the shape of the galactic discs and then estimated the position angle and ellipticity by eye. Note that large variations in the orientation parameters in the very outer points (e.g. UGC 3993, 4458, 8699) can usually be attributed to asymmetries in the light distribution of the galaxy or to imperfect flat-fielding; these variations were generally not considered real. The adopted values for the position angle and ellipticity are indicated with the dashed lines in Figure B1 and are listed in Columns (6) and (7) in Table A2.

From the ellipticity, we determined the inclination of the galaxies using the standard formula

$$\cos^2 i = \frac{(1-\epsilon)^2 - q_0^2}{1 - q_0^2}, \quad (3)$$

with q_0 the intrinsic flattening of the disc, for which we assumed a value of 0.2 (cf. de Grijs 1998). The derived values are given in Column (8) in Table A2. Note that they are estimates only; if the discs have different intrinsic flattening, or if they are intrinsically elongated rather than axisymmetric, then the true inclination may deviate significantly from these values.

4.2 Surface photometry

Once the orientation parameters were determined, we fixed them for all ellipses and simply measured the average intensities at each radius. The same ellipses were used for the images in different colour bands.

Even though the background subtraction described in Section 3 usually worked quite well, some small residuals always remained. To determine the exact zero-points in the images, as well as their uncertainties, we let the radii of the ellipses expand until they covered the entire images. Thus, intensities were measured not only on the galaxies, but also in annuli centred on, but much larger than, the galaxies. A typical result is shown in Fig. 1.

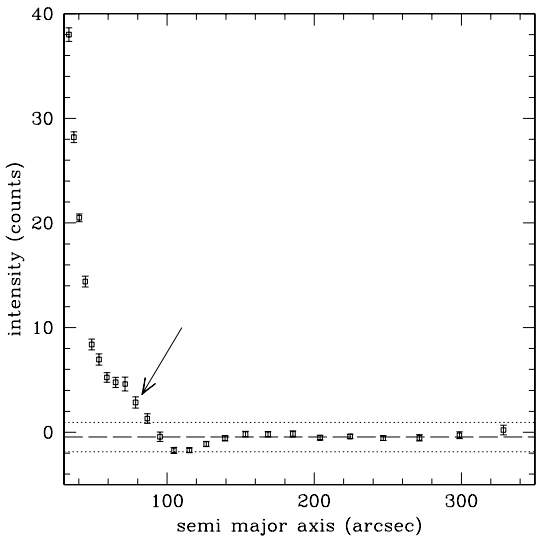

Figure 1. Example of the determination of the exact background level for one of our images. The squares give the average intensities on each ellipse; the error bars give the measurement error. The long-dashed line gives the average intensity of the outer ellipses, which defines the zero-point $I_{\rm bg}$ of the image. In this case, $I_{\rm bg} = -0.46$, indicating that we have slightly over-subtracted the background. The dotted lines give the assumed error in the zero-point. The arrow indicates the outer point with significant flux from the galaxy (see text for details).

In this case, it is clear that no light from the galaxy is detected beyond a radius of about 90 arcsec, so the ellipses outside this radius probe the sky background. The average intensity on the outer ellipses defines the zero-point $I_{\rm bg}$ of the image and is subsequently subtracted from the intensities in the galaxy.

The variation in the intensities on the outer ellipses measures the uncertainty in the zero-point. Note, however, that these outer ellipses cover large parts of the image, such that small-scale irregularities in the background are averaged out. To account for irregularities at smaller scales as well, we adopted for the zero-point uncertainty $\sigma_{\rm bg}$ *twice* the rms variation in the intensities of the outer ellipses. In Table A1, we give the magnitude level $\mu_{3\sigma}$ corresponding to $3\sigma_{\rm bg}$ above the sky; the average values are 26.95, 26.07 and 24.26 mag arcsec^{-2} in the *B*-, *R*- and *I*-band images, respectively.

The errors on the measured intensities in the galaxy are now given by the quadratic sum of the measurement error $\Delta I_{\rm m}(r)$ and the zero-point error $\sigma_{\rm bg}$:

$$\sigma_I(r) = \sqrt{\Delta I_{\rm m}(r)^2 + \sigma_{\rm bg}^2}. \quad (4)$$

Finally, the intensities and corresponding errors were calibrated and converted to surface magnitudes using the transformations determined in Section 3. Only points with intensities larger than $2\sigma_{\rm bg}$ were considered. The resulting photometric profiles are shown in the top middle panels on the first row of the figures in Appendix B. In the bottom middle panels on the first row of the figures, the colour profiles are shown. The errors on the points are given by the quadratic sum of the errors on the individual bands. Points are only shown when the total error is smaller than 0.5 mag.

4.3 Deviations from axisymmetry

In addition to the average intensity on each ellipse, we also measured the higher order harmonic components to study deviations from perfect axisymmetry. The intensity distribution along each ellipse was decomposed into a Fourier series of the following form:

$$I(\alpha) = I_0 + I_1 \cos(\alpha + \phi_1) + I_2 \cos[2(\alpha + \phi_2)] + \cdots, \quad (5)$$

where α is the azimuthal angle along the ellipse, I_0 is the average intensity on the ellipse and I_1 and I_2 measure the strength of the $m = 1$ and 2 Fourier components, respectively. Thus, a high value for I_1/I_0 indicates a strongly lopsided light distribution, whereas a high value for I_2/I_0 reveals the presence of a bar or oval distortion.

A statistically significant measurement of these higher order terms in the light distribution requires a higher signal-to-noise ratio than is necessary for the zeroth-order term. The $m = 1$ and 2 terms were therefore only measured on ellipses for which the average intensity was, respectively, $2\sqrt{2}$ and four times $\sigma_{\rm bg}$.

The relative strengths and the phases of the $m = 1$ and 2 components are shown in the bottom four panels on the right-hand side of the first row of the figures in Appendix B.

4.4 Isophotal diameters, effective radii and total magnitudes

For each galaxy and each band, several diameters were derived. D_{25} and $D_{26.5}$ are isophotal diameters, determined at $\mu = 25$ and 26.5 mag arcsec^{-2}, respectively. R_{20}, R_{50} and R_{80} are effective radii, containing, respectively, 20, 50 and 80 per cent of the light. The diameters and effective radii are given in Table A2.

Note that these diameters and effective radii are derived from the photometric profiles as measured on the sky. However, the surface brightnesses of the discs of the galaxies are dimmed by Galactic foreground extinction. On the other hand, the observed surface brightnesses are higher than the true values due to the fact that we observe the galaxies under a non-zero inclination angle. The raw isophotal diameters derived above do therefore not correspond to the same physical surface brightness in the discs of these galaxies. In Table A2, we also give the isophotal diameters $D_{25}^{\rm c}$ and $D_{26.5}^{\rm c}$ that correspond to face-on, extinction corrected levels of $\mu = 25$ and 26.5 mag arcsec^{-2}. The correction for inclination was performed assuming that the galactic discs are optically thin; no corrections were made for internal extinction caused by dust in the galactic discs themselves. The corrections for Galactic foreground extinction were performed using the values from Schlegel, Finkbeiner & Davis (1998).

Total magnitudes cannot be derived from the images directly, as large parts of the images are sometimes masked to remove foreground stars, background galaxies, etc. (Section 3), such that the masked images contain flux from parts of the galaxies only. To correct for this effect, model images were created, based on the photometric profiles derived in Section 4.2, interpolating over the masked regions. From these model images, two apparent magnitudes were derived. $m_{\rm lim}$ is the total magnitude within the last measured point in the photometric profile; m_{25} is the apparent magnitude within the 25th mag arcsec^{-2} isophotal diameter D_{25}. The errors in the total magnitudes are usually dominated by the uncertainty $\sigma_{\rm phot}$ in the photometric calibrations (equation 2, Column 7 in Table A1), with small contributions from the zero-point uncertainty $\sigma_{\rm bg}$ and Poisson errors.

The corresponding absolute magnitudes $M_{\rm lim}$ and M_{25} were determined using the distances as given in Table 1 and were corrected for Galactic foreground extinction using the values from Schlegel et al. (1998).

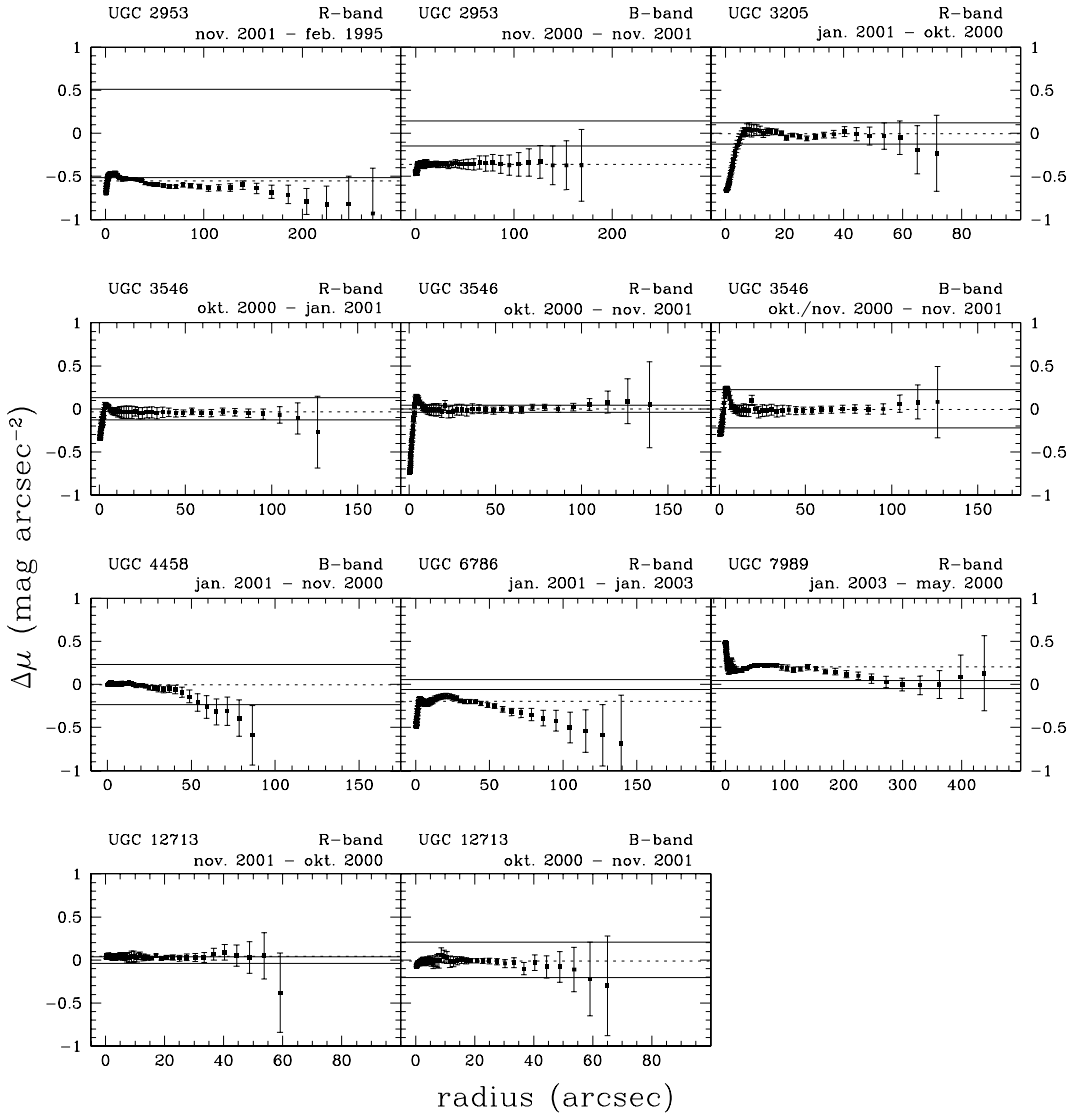

Figure 2. Internal comparison of the photometric profiles. Data points show the difference between photometric profiles from multiple observations of the same galaxy. The observations which are compared are indicated above each panel (see Table A1 for details). Error bars give the combined errors on each point. Dashed lines give the weighted average of the points which are not affected by seeing differences. Solid lines give the combined 1σ photometric errors.

5 INTERNAL COMPARISON OF PHOTOMETRIC PROFILES

Several galaxies were observed during different nights and with different telescopes (see Table A1). For each of these cases, only the best data are shown in Appendix B and are listed in Tables A2 and A3. The data from the other observations have been used to assess the quality of our data and the reliability of the derived errors. These observations were reduced independently, following the same steps as for the main observations. The same masks were used, however, for all images (Section 3), to make sure that measured surface brightnesses correspond to the same regions in all images. Similarly, the same position angles and ellipticities were used to derive the photometric profiles.

In Fig. 2, we compare the photometric profiles for all the galaxies with multiple observations. In most cases, the independently derived profiles agree very well, but there are also some cases with significant differences.

Errors in the photometric calibrations lead to constant offsets in a profile but leave its shape unchanged. Indeed, systematic offsets between two profiles are seen for some galaxies in Fig. 2 (the dotted lines give the weighted average of the data points), but in most cases, these offsets fall within the combined 1σ photometric errors (solid lines). In a few cases, the offsets are larger than to be expected (notably UGC 2953, 6786 and 7989[3]). In the case of UGC 2953, the differences between the independent observations can be explained as the result of non-photometric conditions during the nights of the comparison observations. In Tables A1, A3 and A4, we have marked all observations that were done under non-photometric conditions. Note that non-photometric conditions do not affect the shapes of the

[3] The analysis in this section includes two galaxies, UGC 7989 and 12713, which were observed during the same runs as the other galaxies in our sample, but which are not included in the remainder of this study. They are only shown here as additional comparison material.

photometric profiles. Scalelengths, effective radii, bulge–disc ratios, etc. can still be accurately measured on such nights. Furthermore, in many cases, galaxies that were observed under non-photometric conditions were later re-observed with short exposure times; these short exposures were then used to calibrate the deep images taken before and accurate photometry could still be achieved.

The offsets for UGC 6786 and 7989 are probably caused by differences between the filter transmission curves used for the observations on the JKT and the MDM telescope. Note that the offsets between the JKT and MDM profiles are equally large (0.20 mag arcsec^{-2}) for both UGC 6786 and 7989; this strengthens the interpretation of the offsets as a result of filter differences.

Apart from the systematic offsets between the profiles, random point-to-point variations are generally small, except for the inner few arcsec where differences in seeing between the observations lead to artificially large discrepancies. In some cases, errors in the sky-level determination lead to differences in the outer points of the compared profiles, but they are generally within the errors derived as described in Section 4.2. The largest sky-subtraction errors are seen in UGC 4458, where the outer points of the two compared profiles disagree at a level of two times the combined 1σ errors. Given the number of profiles compared here, one case of 2σ disagreement is to be expected. The only cases where we observe significant differences between the profiles that cannot be attributed to seeing effects or uncertainties in the sky level are the profiles which were observed with different telescopes (*R*-band observations of UGC 2953, 6786 and 7989); as above, these differences can probably be attributed to the different filters which were used for the observations under comparison here.

In conclusion, for galaxies that were observed under photometric conditions, the photometric errors listed in Table A1 seem to be reliable; for non-photometric observations the errors are lower limits. The errors on individual data points in our photometric profiles are also realistic and account well for the uncertainties in the determination of the sky level. Photometric profiles which were derived from images observed with the INT or MDM telescope show small deviations ($\sim$0.1–0.2 mag arcsec^{-2}) compared to the profiles derived from the JKT images. The deviations manifest both as systematic offsets between the profiles and as point-to-point variations within the profiles. These differences are probably caused by differences in the filters used for the observations.

6 BULGE–DISC DECOMPOSITIONS

Many methods exist to decompose the light of spiral galaxies into contributions from bulges and discs. Traditionally, the decomposition is performed on the photometric profiles directly, fitting them with the sum of an exponential disc and a certain profile for the bulge (usually an $r^{1/4}$, exponential or general Sérsic profile). As this is a 1D procedure, it is quick and can therefore be used to study large samples of galaxies in short time-spans (e.g. Baggett, Baggett & Anderson 1998; Graham 2001; MacArthur, Courteau & Holtzman 2003). However, photometric profiles suffer from projection effects. The observed intensity at each point in a galaxy is a superposition of light from the bulge and disc. Because they have different intrinsic shapes, the contributions from both components come from different radii when the galaxy is observed under a non-zero inclination angle, and the average intensity along a given isophote is generally not directly related to the true mean brightness at that radius. Thus, deriving bulge and disc parameters from azimuthally averaged photometric profiles will lead to systematic errors. A proper treatment of the projection effects requires a full 2D decomposition technique

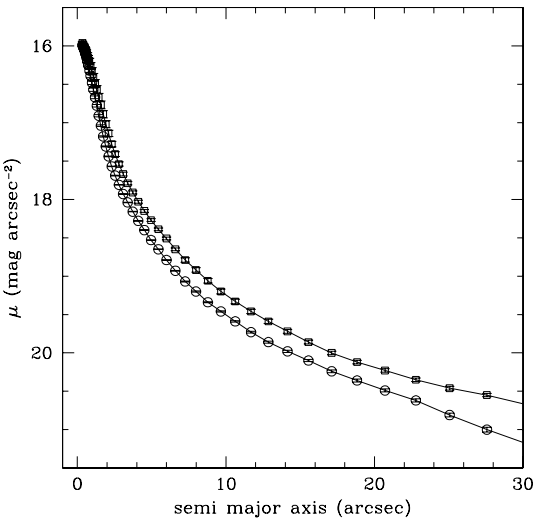

Figure 3. The influence of projection effects on the central *R*-band photometric profile of UGC 6786. The profile shown with squares is derived using the standard method, i.e. the intensities are measured along ellipses with ellipticity fixed at the value of the outer regions. The circles denote the profile when measured along ellipses with an ellipticity which better represents the isophotes of the bulge.

(e.g. Byun & Freeman 1995; de Jong et al. 2004; Laurikainen, Salo & Buta 2005).

The projection effects described above are particularly severe in the type of galaxies studied here, which have often large and luminous bulges. As an illustration, we show in Fig. 3 two *R*-band photometric profiles of the central part of the bulge-dominated galaxy UGC 6786. The profile shown with squares is derived following our standard procedures of Section 4.2, that is, it shows the average intensities measured along ellipses with the ellipticity fixed at the value of the outer regions. The circles show the intensities when measured along ellipses with a much lower ellipticity, which is more representative of the isophotes in the central, bulge-dominated region. Clearly, the bulge of UGC 6786 is more centrally concentrated than is shown by our standard photometric profile; any structural parameters of the bulges derived directly from our photometric profiles will be severely affected by systematic errors.

Another problem with bulge–disc decompositions is the degeneracy that exists between the different parameters (MacArthur et al. 2003; de Jong et al. 2004). The data can often be fitted by different combinations of parameters, so that it can be difficult to reach unambiguous conclusions about the true values.

To overcome the difficulties mentioned above, we have developed a hands-on, interactive procedure that uses the full 2D information from the images to separate them into bulge and disc components. Our method bears some similarities with the one used by Palunas & Williams (2000) and can be summarized as follows. We model the bulges as flattened axisymmetric spheroids, with intrinsic axis ratios q_b and general Sérsic photometric profiles characterized by effective radius and magnitude r_e and μ_e and shape parameter n (Sérsic 1968). The bulge parameters are determined from images where an initial estimate for the discs has been subtracted. Based on the fitted parameters, model images of the bulges are created and subtracted from the original images. All light in these images is then assumed to originate from the discs, and their photometric profiles are used to derive the disc light distributions.

A more detailed description of the separate steps is given in the following sections.

6.1 Bulge parameters

The first step in our procedure consists of deriving initial estimates for the bulge and disc parameters from an analytic fit to the photometric profile. As discussed above, the central, bulge-dominated parts of the photometric profiles suffer from projection effects. In the outer parts, however, the profile is usually dominated by the flat disc, and projection effects are not an issue. Thus, the initial estimates for the disc are generally sufficiently reliable for the next step.

Based on the initial estimates, an initial model image of the disc component is created by extrapolating the fitted disc profile inwards. This model image is then subtracted from the original image to obtain an image with, to first order, bulge-light only.

From the resulting image, the bulge parameters can be obtained. We first determine the flattening of the bulge by fitting ellipses to the *R*-band bulge image with ellipticity and position angle as free parameters. In most cases, the position angle of the bulge isophotes is close to the value derived for the outer disc, indicating that the bulge is a flattened spheroid with the plane of symmetry coinciding with that of the disc. In a few cases, the position angle in the centre differs from the outer values, indicating the presence of a nuclear bar or other triaxial structure. The presence of these non-axisymmetric structures is ignored in the following; we model all bulges as oblate spheroids that are aligned with the outer disc and we simply average out any non-axisymmetric structures along the isophotes in the next step. Because the bulges are more vertically extended than the surrounding discs, their ellipticities are generally lower than those found for the outer discs. From the average ellipticity ϵ_b of the bulge isophotes, the intrinsic flattening of the bulge can be determined by rewriting equation (3) as

$$q_\mathrm{b}^2 = \frac{(1-\epsilon_\mathrm{b})^2 - \cos^2 i}{1-\cos^2 i}. \tag{6}$$

Here, q_b is the intrinsic axis ratio of the bulge and i is the inclination of the system, as derived in Section 4.1.

We next derive photometric profiles for the bulge in all available colour bands by measuring the average intensities on concentric ellipses with fixed ellipticity ϵ_b. Intensities are only measured inside the radius where the bulge and disc intensities from the original image are equal. The resulting profiles are shown with the data points in Figure B1.

To extrapolate the contribution of the bulge to larger radii, we fitted the profiles with a general Sérsic light profile (Sérsic 1968):

$$I_\mathrm{b}(r) = I_{0,\mathrm{b}} \exp\left[-\left(\frac{r}{r_0}\right)^{1/n}\right]. \tag{7}$$

Here, $I_{0,\mathrm{b}}$ is the central surface brightness and r_0 is the characteristic radius. n is a shape parameter that describes the curvature of the profile in a radius–magnitude plot. For $n = 4$, equation (7) reduces to the well-known De Vaucouleurs profile (de Vaucouleurs 1948), whereas $n = 1$ describes a simple exponential profile. In the literature, equation (7) is usually written as

$$I_\mathrm{b}(r) = I_\mathrm{e} \exp\left[-b_n\left\{\left(\frac{r}{r_\mathrm{e}}\right)^{1/n} - 1\right\}\right], \tag{8}$$

with $I_\mathrm{e} = \mathrm{e}^{-b_n} I_{0,\mathrm{b}}$ the intensity at the effective radius $r_\mathrm{e} = b_n^n\, r_0$, the radius which encompasses 50 per cent of the light. b_n is a scaling constant that is defined such that it satisfies $\gamma(b_n, 2n) = \frac{1}{2}\Gamma(2n)$, with γ and Γ the incomplete and complete gamma functions, respectively. It can be approximated by $b_n \approx 1.9992\,n - 0.3271$ for $1 < n < 10$ (Graham 2001), but in our fitting procedure, we determined b_n more accurately by numerically solving the equation above.

In magnitudes, equation (8) is written as

$$\mu_\mathrm{b}(r) = \mu_\mathrm{e} + 1.0857\, b_n \left\{\left(\frac{r}{r_\mathrm{e}}\right)^{1/n} - 1\right\}. \tag{9}$$

Before fitting the profile of equation (9) to the observed data, it is corrected for seeing effects using the convolutions from Graham (2001).

The seeing-convolved profile is then fitted to the data using a standard non-linear least-squares algorithm. For the fits to the *B*- and *I*-band profiles, we fixed the parameters n and r_e to the values found for the *R*-band profile, leaving only the effective surface magnitude μ_e free. Thus, we model the bulges as fully mixed systems without colour gradients. Any remaining colour gradients after the subtraction of the bulge influence are attributed to the disc. The fitted profiles are shown as the solid lines in Figure B1.

The fitted bulge parameters ϵ_b, q_b, μ_e, r_e and n are given in Table A4. The effective surface brightness was also corrected for Galactic foreground extinction, using the values from Schlegel et al. (1998); the corrected surface magnitude μ_e^c is listed in Table A4 as well. Finally, a total magnitude was derived by integrating equation (7) to infinity; the resulting values m_b and M_b for the apparent and absolute magnitudes are also listed in Table A4. Model images for the bulge in the *R* band, created using the parameters found above, are shown in the bottom left panels in the figures in Appendix B.

6.2 Disc parameters

To measure the light distribution in the disc, the model images of the bulge are subtracted from the original images in each available colour. The resulting *R*-band images are shown in the bottom right panels in the figures in Appendix B.

All remaining light in these images is then assumed to originate from the disc component. This also includes residuals in the bulge-dominated parts, where our fitted analytical profile (equation 8) does not exactly match the observed light distribution. Note, however, that the deviations of the observed bulge profile from the analytic fit are almost always very small compared to the total overdensity of bulge-light over the inner disc (typically 0.05–0.1 versus 2–4 mag). The error caused by attributing the residuals to the disc, instead of to the bulge, will be negligible when calculating the combined dynamical impact of both components.

The radial distribution of the disc light is then determined by measuring the average intensities on the ellipses defined in Section 4.1. The resulting photometric profiles for the disc, outside the bulge–disc transition radius, are shown in the bottom right panels in the figures in Appendix B. In two cases, UGC 6786 and 6787, it was found, after the subtraction of the bulge, that the ellipticity derived from the original image did not accurately represent the inclination of the disc. In these two cases, the bulges are so dominant that, in the original images, they influence the shape of the isophotes even in the outer parts. The correct inclination angle of the discs could therefore only be determined after the subtraction of the bulge, and for the final disc profile, we used values different from the ones listed in Table A2 (see individual notes in Section 8). The corrected inclination angle was also used to recalculate the flattening of the bulges for these galaxies (equation 6).

Finally, exponential profiles were fitted to the observed disc profiles:

$$I_{\rm d}(r) = I_{0,\rm d} \exp\left(-\frac{r}{h}\right), \tag{10}$$

or in magnitudes

$$\mu_{\rm d}(r) = \mu_{0,\rm d} + 1.0857\left(\frac{r}{h}\right), \tag{11}$$

with $I_{0,\rm d}$ and $\mu_{0,\rm d}$ the central surface brightness, and h the radial scalelength. Only points outside the bulge–disc transition radius were used for the fit. The resulting parameters are listed in Table A4; the corresponding profiles are shown as the solid lines in Figure B1. In Table A4, we also list $\mu^c_{0,\rm d}$, the central surface brightness corrected for inclination and Galactic foreground extinction. The correction for inclination was performed assuming that the galactic discs are optically thin; the corrections for Galactic foreground extinction were performed using the values from Schlegel et al. (1998).

7 DISCUSSION

The main purpose of the analysis described in this paper is to derive the contribution of the stellar component of our galaxies to their gravitational potential. In a forthcoming paper, we will calculate the contributions of the stellar discs and bulges to the rotation curves, and use the results to constrain the content and distribution of dark matter in our galaxies. Meanwhile, some interesting results concerning the structure and mutual dependence of the bulges and discs of our galaxies can be derived from our study as well. These results are in some ways complementary to the larger studies of e.g. Graham (2001), MacArthur et al. (2003), de Jong et al. (2004), Hunt, Pierini & Giovanardi (2004) and Laurikainen et al. (2005). Below, we discuss the most important points.

7.1 A comparison of bulge and disc parameters

In Fig. 4, we compare the total luminosities, sizes and surface brightnesses of the bulges and discs of the galaxies in our sample with accurate bulge–disc decompositions. It is clear that there is only a weak coupling between the bulge and disc parameters.

There is a weak trend of more luminous discs harbouring more luminous bulges, but the scatter around the relation is large. Moreover, several biases in our sample selection could introduce an artificial correlation: galaxies with a highly luminous bulge and a faint disc might not be classified as disc galaxies, but rather be misidentified as ellipticals. Similarly, luminous discs with faint bulges might not be classified as early-type discs, but rather as late-type spirals. This latter effect is, however, not expected to be as strong as the former, since the morphological type classification is based on other parameters than bulge–disc luminosity ratios as well. Moreover, our sample contains a number of galaxies with high-luminosity discs and faint bulges (e.g. UGC 94, 3205, 3546), which are still clearly recognizable as early-type disc galaxies. UGC 12043 even has no obvious bulge component at all, but is still classified as an S0/a galaxy.

In any case, our results indicate a large range in bulge-to-disc (BD) luminosity ratio and show that the common belief that early-type disc galaxies have large and luminous bulges does not hold in all cases. This is also visible in the left-hand panel of Fig. 5, where we show the distribution of the BD luminosity ratio for all galaxies in our sample. The average value of $\log(L_{\rm b}/L_{\rm d})$ is -0.23 ± 0.47 in the R band, where the error gives the standard deviation of the sample.

Apart from two galaxies, UGC 624 and 6786, which have unusually large bulges (as measured from their effective radii $r_{\rm e}$), there is a weak correlation between disc scalelength and bulge effective radius (middle panel in Fig. 4). In the following, we will show that UGC 6786 differs from the rest of the sample in many aspects, and we will interpret this in Section 8 as an indication that this galaxy is not really a disc galaxy, but rather an elliptical galaxy with an additional disc of gas and stars. The offset of UGC 624 may be explained as a result of its high inclination with respect to the line of sight. There are indications that the image of this galaxy is significantly affected by dust (note, for example, the strong asymmetry in the centre, visible in the I_1/I_0 lopsidedness parameter, and by eye in the bulge-subtracted image). If there are indeed large amounts of dust present in this galaxy, it is conceivable that they introduce large errors in the shape of the photometric profiles and in the resulting bulge–disc decomposition.

The other galaxies seem to follow the global trend that large bulges reside in large discs, although the scatter is, again, large. In the right-hand panel of Fig. 5, we show the distribution of $r_{\rm e}/h$ for all galaxies in the sample. The average value of this ratio is 0.51 ± 0.72 (the error indicates the standard deviation), but this value is heavily influenced by UGC 6786. The average value for the sample without UGC 6786 is 0.35 ± 0.19, whereas it is further reduced to 0.32 ± 0.15 if UGC 624 is excluded as well. Even this last value is significantly higher than the average $r_{\rm e}/h$ for the late-type spiral galaxies studied by Courteau et al. (1996). It is also higher than the values found by Graham (2001) and MacArthur et al. (2003), who both noted a mild trend of the ratio $r_{\rm e}/h$ increasing towards earlier type spiral galaxies, but only reaching an average of, respectively, 0.21 and 0.24 for the early types.

It is not immediately clear what causes the higher $r_{\rm e}/h$ ratio for our sample, compared to the results of Graham (2001) and MacArthur

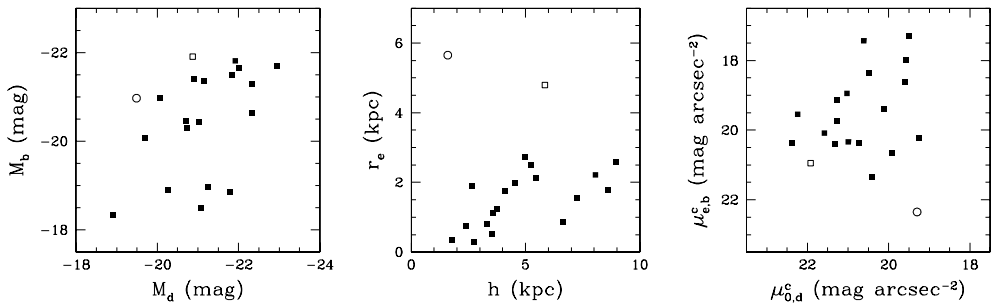

Figure 4. Comparison of the R-band bulge and disc parameters. Left-hand side: absolute magnitudes of bulge versus disc; middle: bulge effective radius versus disc scalelength; right-hand side: bulge effective surface brightness versus disc central surface brightness. The open squares indicate UGC 624, the circles indicate UGC 6786.

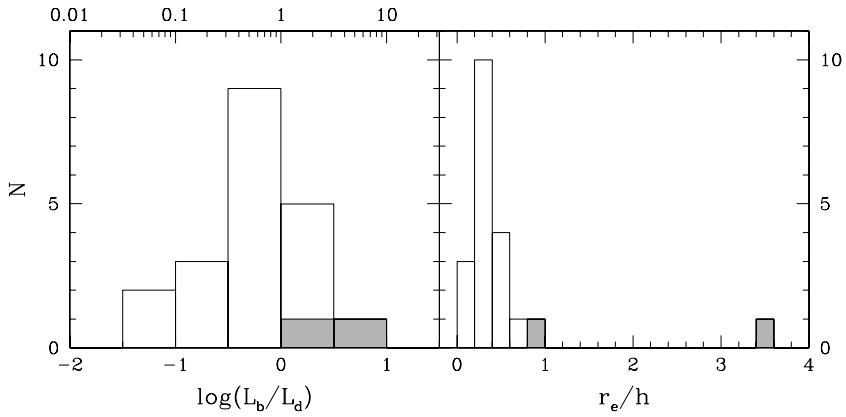

Figure 5. The distribution of the *R*-band BD luminosity ratio (left-hand side) and size ratio (right-hand side) for the galaxies in our sample. Grey shading indicates UGC 624 and 6786.

et al. (2003), but it could well be related to the different decomposition techniques used. We already argued in Section 6.1 that 1D decompositions suffer from systematic effects. Inspection of Fig. 3 shows that, in an extreme case such as UGC 6786, a photometric profile measured along ellipses with ellipticity fixed at the value of the outer disc is shallower than the true light distribution. A simple least-χ^2 1D fit to this profile yields an effective radius for this bulge of 24.0 arcsec, almost a factor of 2 smaller than the value we derived using our 2D method described in Section 6.1 (43.5 arcsec). Although UGC 6786 is an extreme galaxy, it seems likely that the same effect plays a role, perhaps to a lesser extent, in other galaxies as well. Thus, the discrepancy between the average r_e/h ratios of our study and those of the 1D studies of Graham (2001) and MacArthur et al. (2003) strengthens the need for 2D decompositions to recover the bulge parameters accurately, especially in galaxies where the bulges contribute a substantial fraction to the total light (cf. Byun & Freeman 1995; de Jong et al. 2004). Note that our average r_e/h ratio is fully consistent with the study of Khosroshahi, Wadadekar & Kembhavi (2000), who used a 2D decomposition method for a sample of predominantly early-type disc galaxies.

No obvious trend is visible between the surface brightnesses of the bulges and discs in our sample (right-hand panel in fig. 4, cf. Hunt et al. 2004).

7.2 Correlations between different bulge parameters

Previous studies, such as the ones by Khosroshahi et al. (2000), Graham (2001) and de Jong et al. (2004), have revealed several correlations between the different parameters which characterize the bulges. In Fig. 6, we study several of these correlations for our galaxies.

In this figure (Fig. 6, Panel a), the effective radius shows a clear correlation with the total luminosity of the bulge. This is not very surprising, and simply shows that larger bulges are more luminous.

A priori less expected is the relation between the Sérsic index n and the total luminosity of the bulges (Panel d): luminous bulges have predominantly higher n values than their low-luminosity counterparts. This trend was noted before by e.g. Andredakis et al. (1995), Khosroshahi et al. (2000) and Graham (2001), and is also observed in elliptical galaxies (e.g. Caon, Capaccioli & D'Onofrio 1993; Young & Currie 1994; Jerjen, Binggeli & Freeman 2000). It should, however, be approached with some caution, as there may be a selection effect at play. Low-luminosity bulges are generally small (Panel a) and in many cases, their effective radii are only a few arcsec on the sky (see also Table A4). In such cases, the seeing will smear out any sharp peaks in the light profiles and, even though we deconvolve our bulge profiles when fitting the Sérsic model, the n value will effectively be lowered (Trujillo et al. 2001a). Thus, the apparent correlation in Panel (d) may be partly artificial, and sub-arcsec images would be required to confirm the trend at the low-luminosity end (cf. Balcells et al. 2003).

The bulges in our sample span the full range from exponential light profiles ($n \approx 1$) to De Vaucouleurs ($n \approx 4$), with UGC 6786 lying out at $n = 5.5$. A histogram of the distribution is shown in Fig. 7. The average value of n for the entire sample is 2.5 ± 1.1, where the error gives the standard deviation of the sample; for the sample without UGC 6786, this becomes $\langle n \rangle = 2.3 \pm 0.9$. These values are fully consistent with previous results from e.g. Andredakis et al. (1995), de Jong (1996a), Graham (2001) and Hunt et al. (2004) and confirm the view that the bulges of early-type disc galaxies form, at least as far as their n values is concerned, an intermediate population between elliptical galaxies, which have n around four but up to 15 in extreme cases (Caon et al. 1993; de Jong et al. 2004), and late-type galaxy bulges, which usually have exponential or even steeper profiles (e.g. de Jong 1996a; MacArthur et al. 2003).

The three fundamental bulge parameters from equation (9), μ_e, r_e and n are all clearly correlated (Panels c, e and f in Fig. 6, cf. Khosroshahi et al. 2000, de Jong et al. 2004, Hunt et al. 2004), but the selection effect described above may be important here as well: seeing effects may introduce a bias for small bulges towards lower n. Furthermore, the correlations may partly be caused by the definition of these parameters which intrinsically couple them. Bulges with higher n values have a shallower light profile at large radii, but with a suitable choice of the central surface brightness and effective radius, the profile can look relatively similar to that of low-n bulges in the inner parts. Such high-n bulges will have a larger effective radius r_e than low-n bulges, and the surface brightness μ_e at that radius will be lower. These are exactly the trends which are visible in Fig. 6.

Parameter coupling alone cannot, however, explain the correlations between the bulge parameters. This can be appreciated, for example, by considering instead of the effective surface brightness the *central* surface brightness μ_0. In Fig. 8, we show that the fitted central bulge surface brightness is highly variable, with a similar width in the distribution as for the effective surface brightness μ_e. Moreover, it is strongly correlated with the Sérsic shape parameter as well. Thus, for a given n, bulges occupy a distinct region in

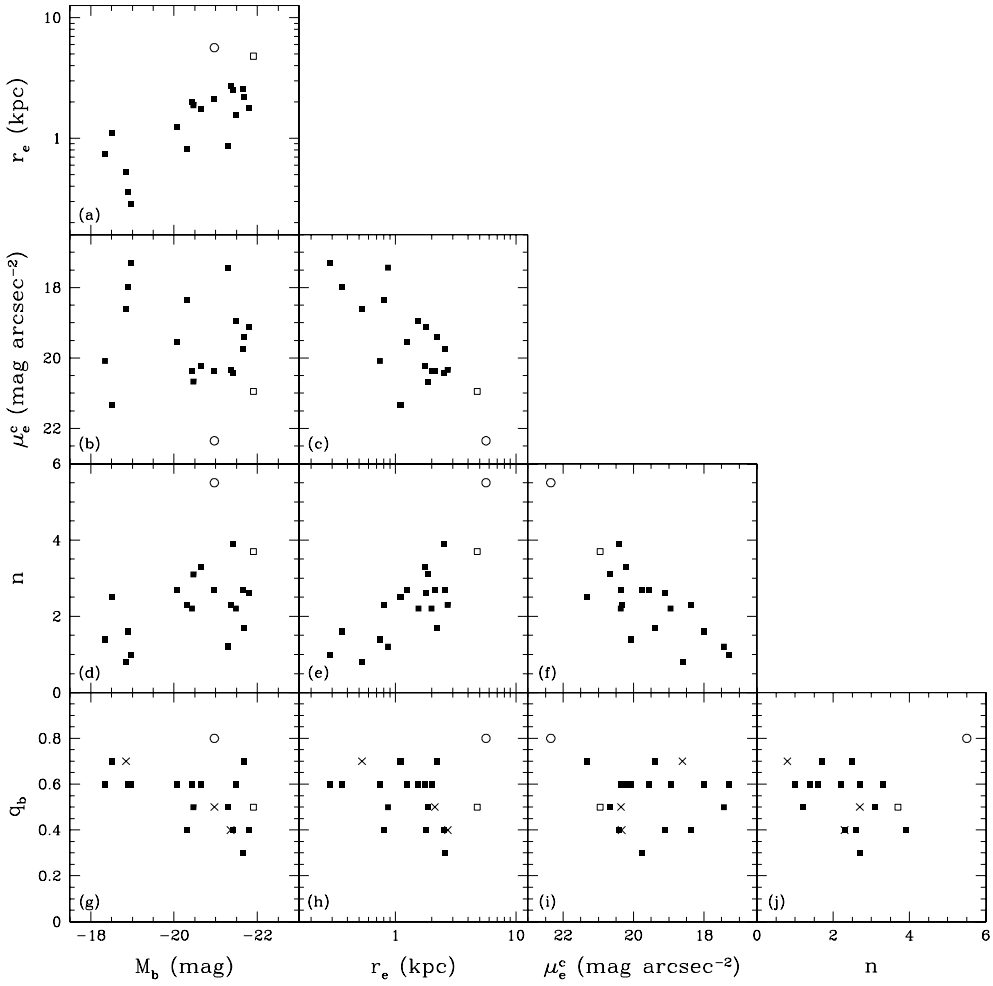

Figure 6. Correlations between different bulge parameters: total magnitude M_b, effective radius r_e, effective surface brightness μ_e^c (corrected for Galactic foreground extinction), Sérsic parameter n and intrinsic axis ratio q_b. All data refer to the *R*-band images. The open squares indicate UGC 624 and the circles indicate UGC 6786. The crosses in the bottom panels indicate bulges where the determination of the intrinsic flattening of the bulge was difficult (UGC 2916, 3205 and 3993; see Table A4).

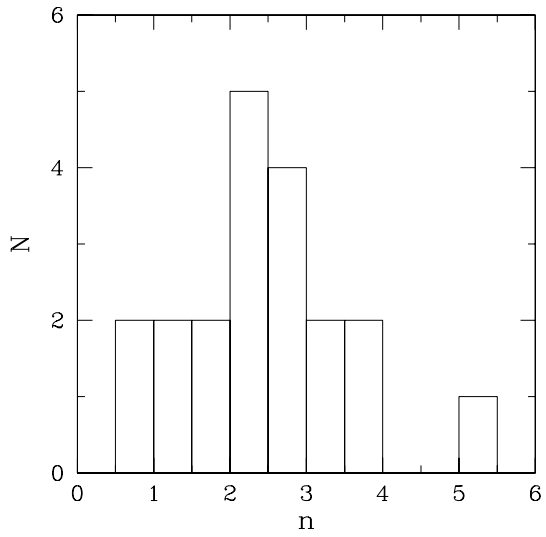

Figure 7. The distribution of the Sérsic n parameter for the bulges in our sample. The numbers were derived from the *R*-band data.

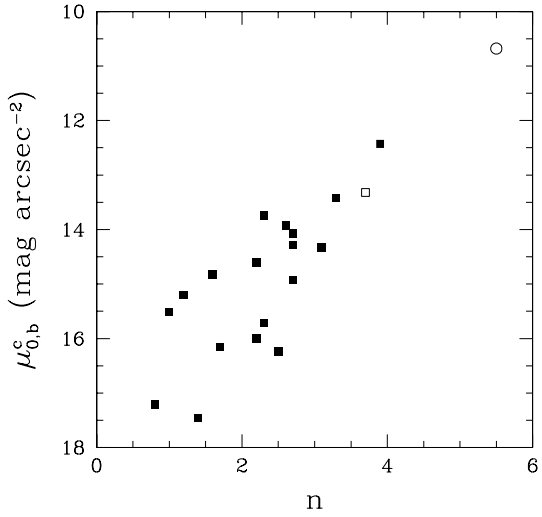

Figure 8. The correlation between Sérsic n parameter and fitted central surface brightness μ_0 (corrected for Galactic foreground extinction) for the bulges in our sample. All data are derived from the *R*-band images.

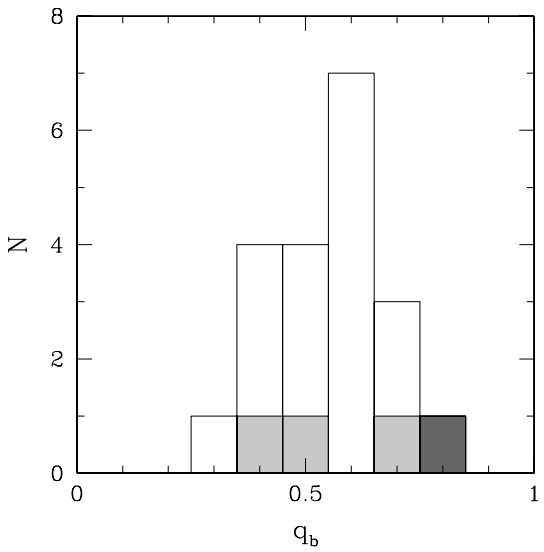

Figure 9. The distribution of the intrinsic axis ratios q_b of the bulges in our sample. All values were derived from the *R*-band data. The white histogram shows the distribution for the entire sample, the light grey shading indicates galaxies where the determination of q_b was particularly difficult (UGC 2916, 3205 and 3993; see Table A4). Dark shading indicates UGC 6786.

surface brightness space. The correlations between the bulge parameters are therefore real and must have a true physical basis (cf. Trujillo, Graham & Caon 2001b).

There seems to be a weak trend between the flattening of the bulges and their total luminosity, more luminous bulges being on average more flattened than low-luminosity bulges (Panel g in Fig. 6). This result is somewhat surprising, since previous studies had found that flat 'pseudo-bulges' are more common in late-type spiral galaxies than in early-type disc galaxies (Kormendy 1993; Kormendy & Kennicutt 2004, and references therein). One would thus expect the most spherical bulges in our sample to be the most luminous, but this is clearly not the case.

It is important to note that the uncertainties in individual measurements of the intrinsic axis ratio of the bulge are large. In several cases, the ellipticity of the bulge isophotes is not constant with radius, and it is problematic to assign a unique value to the apparent axis ratio of the bulge. In other cases, where the bulges are small, seeing effects may lead to biases as well. Finally, in galaxies that are close to face-on, there is little leverage on the problem, as different intrinsic axis ratios lead to very minor changes in the observed image. The three galaxies where the determination of the bulge flattening was particularly difficult (UGC 2916, 3205 and 3993) are indicated with crosses in the bottom panels in Fig. 6. In spite of all these problems, the correlation in Panel (g) is suggestive, and the uncertain data points do not appear to alter it. There seems to be a genuine trend of more luminous bulges being flatter than less luminous ones.

Finally, the distribution of the intrinsic axis ratios q_b for our entire sample of bulges is shown in Fig. 9. The average value for the sample is $\langle q_b \rangle = 0.55 \pm 0.12$, where the error gives the standard deviation of the sample. Exclusion of the three uncertain values does not lead to different values. Note that none of the galaxies in our sample harbours a truly spherical bulge. Furthermore, the least-flattened bulge is that of UGC 6786, which differs from the rest of the sample in many respects (see discussion above) and seems to be more resemblant of an elliptical galaxy with a small disc of stars and gas (see also the note in Section 8). All other bulges have an intrinsic axis ratio of 0.7 or less.

7.3 Colour gradients

It has long been known that many spiral galaxies do not have a uniform colour over their entire disc, but instead become bluer towards larger radii (de Vaucouleurs 1961; de Jong 1996b; Matthews, Gallagher & van Driel 1999). Such colour gradients have been interpreted in the past as a result of radial variations in the dust content and star formation history (SFH) in the discs of spiral galaxies. de Jong (1996b) concluded, based on detailed radiative transfer and stellar synthesis models, that dust reddening plays only a minor role and that most of the colour gradients are due to 'a combined stellar age and metallicity gradient across the disc, with the outer regions being younger and of lower metallicity'. On the other hand, Möllenhoff, Popescu & Tuffs (2006) recently argued that 'the tendency for apparent scalelength to increase with decreasing wavelength is primarily due to the effects of dust'. Clearly, the underlying mechanisms causing the colour gradients are not fully understood yet.

Here, we investigate whether colour differences between the bulges and the discs are responsible for (part of) the observed colour gradients in our galaxies.

Inspection of Figure B1 shows that many galaxies in our sample have colour gradients; most galaxies become bluer towards larger radii. There are, however, also galaxies which show no evidence for colour variations, or which become redder towards large radii (e.g. UGC 89, 2953). It is important to note that the error bars on the colour profiles become large in the outer regions of the galaxies, predominantly as a result of the uncertainties in the determination of the background level of the images. Although we attempted to determine the background level in our images as accurately as possible and we tried to include its uncertainty in the error bars of our photometric profiles (see Section 4.2), it is possible that the large colour variations in the outer parts of e.g. UGC 6787 are the result of incorrect background levels in one of the colour bands. Colour variations in the bright inner regions of the galaxies cannot be explained by an improper background determination and must be real.

The results from our bulge–disc decompositions indicate that the bulges of our galaxies are on average significantly redder than the discs surrounding them (see Fig. 10). The average *B*–*R* colour difference between the bulges and discs is $\langle (B-R)_{\rm bulge} - (B-R)_{\rm disc} \rangle = 0.43 \pm 0.30$, where the error gives the standard deviation of the sample. This colour difference between bulges and discs is, in most cases, at least partly responsible for the observed colour gradients: the relative contribution of the red bulge light declines towards larger radii, at the cost of an increasing contribution of bluer disc light. Good examples of this effect are UGC 94, 1541, 5253 and 11670.

However, the colour differences between bulges and discs are not sufficient to explain all radial colour gradients. In some cases, the bulge-subtracted images (shown at the bottom right in the figures in Appendix B) do not contain any remaining colour variations, showing that indeed the colour gradients in the original images were caused by the influence of the bulges (e.g. UGC 2916, 9133, 11670). But in most cases, the bulge-subtracted images still contain colour gradients and become bluer towards larger radii (e.g. UGC 2487, 3205, 3993, 6787). Thus, our results show that not only are bulges on average redder than their surrounding discs, the discs themselves are also bluer in the outer parts than at smaller radii. If De Jong's conclusion was correct that dust reddening plays only a minor role

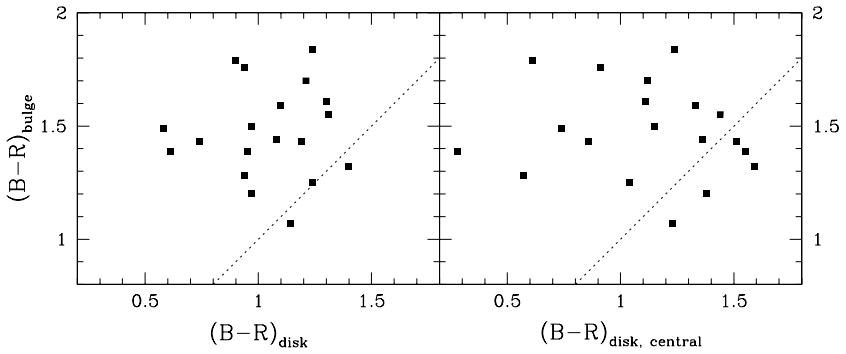

Figure 10. Bulge *B*–*R* colour versus disc colour. In the left-hand panel, the bulge colour is plotted versus the integrated disc colour; in the right-hand panel, it is plotted against the fitted central disc colour, $\mu^c_{0,B} - \mu^c_{0,R}$. The dashed line gives the locations of equal colour. All colours are corrected for Galactic foreground extinction.

in the colour gradients (de Jong 1996b), then our results indicate that the stars in the bulges were on average formed earlier than those in the disc (or have higher metallicity), and that in the discs themselves, the SFH and metallicity vary with radius (with the stars in the outer regions being younger and/or having lower metallicity).

8 NOTES ON INDIVIDUAL GALAXIES

UGC 89 (NGC 23) has a relatively small ($r_e/h = 0.13$) but bright bulge (central surface brightness $\mu_{c,R} = 15.9$ mag arcsec^{-2}). The presence of the strong bar complicates the determination of the bulge parameters, as it dominates the light distribution to very small radii. In particular, the ellipticity of the isophotes does not reach a constant value in the bulge region, so we were forced to estimate the bulge ellipticity ϵ_b by eye. The bar is also responsible for the characteristic 'dip' around $r = 35$ arcsec in the surface brightness profiles.

UGC 94 (NGC 26) has a very low BD luminosity ratio of $L_b/L_d = 0.09$ in *R* (0.04 in B). The low luminosity of the bulge is caused by its low effective surface brightness ($\mu^c_e = 21.4$ mag arcsec^{-2} in the *R* band), while its effective radius is normal ($r_e/h = 0.31$). Of all bulges in our sample, this one lies furthest to the bottom left in Panel (b) of Fig. 6 (μ^c_e versus M_b). Although UGC 94 is not classified as a barred galaxy, it has a small but distinct bar in the centre, oriented approximately east–west.

UGC 624 (NGC 338) has a relatively large and luminous bulge ($r_e/h = 0.82$, $L_{b,R}/L_{d,R} = 2.60$; see Fig. 4). These extreme properties may, however, be a result of the poor bulge–disc decomposition for this galaxy. The combination of an exponential disc and Sérsic bulge seems a rather inadequate description of this galaxy and the extreme bulge properties may be simply an artefact caused by the fitting of an inappropriate model to the data. Part of the problem with UGC 624 may be the high inclination and resulting dust extinction. There are strong indications for dust extinction in the centre (note, for example, the strong asymmetry in the centre, visible in the I_1/I_0 lopsidedness parameter, and by eye in the bulge-subtracted image). It is not inconceivable that the peculiar shape of the luminosity profile of this galaxy is at least partly caused by dust extinction.

UGC 1541 (NGC 797) has a distinct bar which causes the typical 'bump' in the luminosity profile around 40 arcsec. To the west, at the end of the spiral arm, a small companion elliptical galaxy is visible (cf. Zwicky & Zwicky 1971). The light of this companion was masked out for the measurement of the luminosity profile and the subsequent bulge–disc decomposition.

The *R*-band image of this galaxy, which is shown in Figure B1, was taken in windy conditions. As a result, the telescope suffered from mild vibrations, causing the PSF to be elongated, roughly along the east–west direction. To avoid errors due to this effect, we measured the position angle and ellipticity of the bulge from the *B*-band image. Outside the region affected by the PSF elongation, the *R*-band image is consistent with the bulge orientation thus derived.

UGC 2487 (NGC 1167) is the most luminous galaxy in our sample ($M_{\mathrm{lim},R} = -23.24$). It is an almost perfect superposition of an exponential disc and a Sérsic bulge; the residuals with respect to the fitted bulge and disc profiles are less than 0.05 mag arcsec^{-2} everywhere. Some very faint spiral structure is visible in the disc.

UGC 2916 has a nuclear bar; the ellipticity of the isophotes in the centre does not represent the shape of the bulge and we were forced to estimate the bulge ellipticity ϵ_b by eye. As a result, the derived intrinsic axis ratio of the bulge is uncertain. The colour gradient in this galaxy can be fully explained by the colour difference between the bulge and disc; the colour of the bulge-subtracted image does not vary with radius.

UGC 2953 (IC 356) is a large and well-resolved galaxy on the sky, but it is relatively nearby ($D = 15.1$ Mpc) and the physical dimensions are rather average for our sample ($h = 4.1$ kpc). The decomposition into exponential disc and Sérsic bulge is almost perfect, with residuals less than 0.1 mag arcsec^{-2} almost everywhere. It is also one of the most symmetric galaxies in our sample, without any strong lopsided or oval distortions.

UGC 3205 has the lowest *R*-band BD luminosity ratio of all galaxies in our sample ($L_b/L_d = 0.07$). Its bulge is also very small compared to the surrounding disc ($r_e/h = 0.15$) and is only barely resolved in our images ($r_e = 2.2$ arcsec, 1.7 times the seeing of the *R*-band observations). As a result, the fitted Sérsic parameter *n* and intrinsic axis ratio q_b for this bulge have a limited accuracy; higher resolution observations are necessary to study the structure of the bulge of this galaxy in detail. Although not classified as a barred galaxy, UGC 3205 has a weak bar, roughly oriented east–west (see also the I_2/I_0 Fourier term in Figure B1). Apart from the bar, the galaxy is highly symmetric. No spiral structure can be seen in our images; a classification as S0 seems more appropriate than the Sab from the UGC.

UGC 3546 (NGC 2273) has the smallest bulge of all galaxies in our sample, both in absolute terms ($r_e = 0.29$ kpc) as relative to the surrounding disc ($r_e/h = 0.10$), but due to its high surface brightness, the BD luminosity ratio is larger than in UGC 3205 ($L_b/L_d = 0.12$). The bulge is embedded in a distinct bar; two spiral arms emanate from the ends of it and form a ring in the outer parts

(cf. van Driel & Buta 1991). In the very inner parts, a secondary bar seems present, but high-resolution observations with *HST* by Erwin & Sparke (2003) showed that it is actually a nuclear ring with a star-forming spiral inside. UGC 3546 has a Seyfert 2 nucleus (Huchra, Wyatt & Davis 1982) and has been extensively studied at radio wavelengths (e.g. Ulvestad & Wilson 1984; Nagar et al. 1999). This galaxy was observed during three different runs in R and two runs in B, enabling a thorough check on the internal consistency of our observations and data reduction techniques (see Section 5); all observations were found to be fully consistent.

UGC 3580 is a relatively small and low-luminosity galaxy, with an absolute R-band magnitude of -19.42 and an R-band disc scalelength of 2.4 kpc. It has an irregular appearance and seems strongly affected by dust. Although there is clearly excess light in the centre over the exponential outer disc, this 'bulge' has a patchy light distribution, bearing little resemblance to the smooth spheroids present in most other galaxies in our sample. It is also bluer than the other bulges in our sample [$(B-R)_{\rm b}=1.05$, corrected for Galactic foreground extinction]. Several 'knots' of bright emission are seen in the image as well, presumably regions of active star formation; James et al. (2004) report an equivalent width for Hα + [N II] of 2.9 nm, unusually large for an early-type spiral galaxy, indicating that indeed, this galaxy is actively forming stars. In a forthcoming paper, we will show that the kinematical structure of this galaxy is also different than that of the other galaxies in our sample.

All these facts lead us to assume that UGC 3580 is a (relatively luminous) member of a class of dwarf early-type spiral galaxies, which have distinctly different morphological and kinematical properties than the more common high-luminosity early-type disc galaxies. Other galaxies in our sample which probably belong to this class are UGC 12043 (see below), and UGC 6742 and 12713 (Paper I).

UGC 3993 is an example of a luminous bulge embedded in a LSB disc. The fitted central surface brightness of the disc is 23.2 mag arcsec^{-2} (B band, corrected for Galactic foreground extinction and inclination effects), but the description as an exponential disc is rather poor and this value may not represent the actual surface brightness of the disc in the centre. The bulge-subtracted image in Appendix B shows that the disc is dominated by an inner ring with a radius of approximately 10 arcsec ($\sim$3 kpc). The exact density contrast of this ring with the surrounding disc regions depends quite sensitively on the details of the bulge–disc decomposition; in particular, acceptable decompositions can be performed where the central hole in the disc is not as deep as in our preferred solution. In all solutions, however, there is a clear overdensity at this radius, showing that the ring is a genuine physical feature. In addition to this inner ring, some very faint, filamentary spiral arms are visible in the outer regions of the disc.

Due to the near face-on orientation of this galaxy ($i\approx 23^\circ$), the bulge and disc ellipticity could not be distinguished, and the bulge flattening could only be guessed.

UGC 4458 (NGC 2599) has the second most luminous bulge of all galaxies in our sample ($M_{{\rm b},R}=-21.8$), surpassed only by that of UGC 624 (but see note for that galaxy above). The surrounding disc is highly extended, with an R-band exponential scalelength of 8.6 kpc (second largest of all galaxies in our sample, after UGC 9133). Some filamentary structures can be recognized on the northwest of the disc, either faint spiral arms or shells caused by a merging event.

UGC 5253 (NGC 2985) has a large featureless bulge which is well fitted with an $R^{1/4}$-profile (we find $n=3.9$). However, the ellipticity of the isophotes in the bulge-dominated regions is hardly lower than in the outer, disc-dominated regions, indicating that the bulge is highly flattened; we derive an intrinsic axis ratio of $q_{\rm b}=0.4$. The disc is dominated by beautiful, grand design spiral arms; many 'knots' of bright blue emission can be discerned, presumably star-forming regions (cf. González Delgado et al. 1997).

UGC 6786 (NGC 3900) is in many ways different from the other galaxies in our sample (cf. Section 7). It has the largest and most luminous bulge of all galaxies, compared to the disc ($L_{\rm b}/L_{\rm d}=3.91$, $r_{\rm e}/h=3.54$, all in R) and the Sérsic parameter and intrinsic axis ratio of the bulge are larger than in any other bulge in our sample ($n=5.5$, $q_{\rm b}=0.8$). The bulge is so dominant that the isophotes of the original image do not probe the disc elongation at any radius, so the inclination derived using the standard method (Section 3) was not correct. Only after the subtraction of the bulge could the disc be distinguished properly and could we derive its orientation from the shape of the faint spiral structure. For the derivation of the disc profile and the intrinsic axis ratio of the bulge, we assumed an ellipticity of 0.21, corresponding to an inclination of 69° (close to the kinematical inclination angle of 68°, derived from the H I velocity field).

The resulting disc profile shows a plateau of constant surface density in the centre ($\mu_R\approx 21.5$ mag arcsec^{-2}) and an exponentially decaying profile outside 35 arcsec ($\sim$4.5 kpc). A linear fit to the outer parts of the disc profile yields a scalelength of 12.3 arcsec (1.6 kpc) and a formal central surface brightness of 19.3 mag arcsec^{-2} (R band, corrected for Galactic foreground extinction and inclination). Note, however, that such high surface brightness is in reality not reached in the disc, due to the truncation of the profile around 35 arcsec.

All combined, UGC 6786 does not look like a normal early-type disc galaxy at all, but rather seems to resemble an elliptical galaxy which has acquired a disc of gas and stars. In the recent past, it was discovered that many galaxies, which are classified as ellipticals, harbour small stellar discs (e.g. Rix & White 1990; Scorza & Bender 1995); UGC 6786 could well be an extreme example of such a class of galaxies. There may also be a connection with galaxies such as NGC 3108 or 4278, elliptical galaxies with extended, regularly rotating gas disc around them (Oosterloo et al. 2002; Morganti et al. 2006). It is conceivable that the gas in such galaxies will eventually form stars as well, and in fact, there is some evidence for a very faint stellar disc in the centre of NGC 3108. UGC 6786 may be a similar, but more evolved, system to these galaxies.

UGC 6787 (NGC 3898) suffers from the same problem as UGC 6786: the luminous bulge distorts the isophotes of the disc out to large radii and the standard method to derive the inclination (Section 4.1) cannot be used. Only after the model image of the bulge was subtracted could the disc ellipticity be determined. The final disc photometric profile and the intrinsic axis ratio of the bulge were derived using an inclination of 61°. Note that this is still somewhat lower than the kinematic inclination which we derived from the H I velocity field (69°).

UGC 8699 (NGC 5289) is highly inclined ($i=77^\circ$), but we can still recognize the bright bulge, small bar and surrounding ring. The disc component in this galaxy has a LSB ($\mu^{\rm c}_{0,{\rm d}}=23.4$ mag arcsec^{-2}, B band, corrected for inclination effects and Galactic foreground extinction). The strong asymmetry in the central light distribution is most likely the result of internal absorption by dust; at larger radii, the galaxy is highly symmetric. The sudden change in position angle and ellipticity around 70 arcsec is a result from imperfect flatfielding and is not real.

UGC 9133 (NGC 5533) is a luminous galaxy ($M_R=-22.62$) which can almost perfectly be decomposed in an exponential disc and Sérsic bulge (the residuals being less than 0.1 mag arcsec^{-2} almost everywhere). It has the largest disc scalelength of all galaxies

in our sample ($h_R = 8.9$ kpc). The ellipticity of the bulge is barely lower than that of the disc, implying that the bulge is highly flattened; we derive an intrinsic axis ratio of $q_b = 0.3$. Some faint, filamentary spiral structure is visible in the outer disc.

UGC 11670 (NGC 7013) is a small and relatively low luminosity galaxy ($h_R = 1.8$ kpc, $M_B = -19.20$). It has a large, lens-shaped bar with conspicuous dust lanes running parallel to it. In the outer parts, a diffuse disc with very faint spiral structure can be seen.

UGC 11852 is the most distant galaxy in our sample ($D = 80$ Mpc). It consists of a relatively diffuse bulge embedded in a highly elongated bar. The spiral arms are somewhat irregular and develop into narrow filaments extending to very large radii (barely visible in Figure B1).

UGC 11914 (NGC 7217) is a highly symmetric, nearly face-on galaxy, which can be decomposed well into a Sérsic bulge and an exponential disc. The bulge is relatively large, compared to the disc ($r_e/h = 0.71$). The residuals with respect to the model components are small, except for a distinct ring of blue stars which causes excess light at a radius of approximately 75 arcsec ($\approx$5.5 kpc; cf. Buta et al. 1995; Verdes-Montenegro, Bosma & Athanassoula 1995). This ring coincides with an enhanced surface density of neutral gas (Paper I) and contains many star-forming regions (Pogge 1989; Battinelli et al. 2000). However, as discussed in Paper I, the gas surface densities are below the star formation threshold from Kennicutt (1989), so it is puzzling how this galaxy can sustain its large-scale star formation activity.

Note that our BD luminosity ratio for UGC 11914 is much lower than the value derived by Buta et al. (1995) (0.58 versus 2.3, both *B* band); this difference is presumably caused by the fact that they used an $R^{1/4}$-profile for the bulge, whereas we left the Sérsic index free in the fits. Our fitted bulge profile has $n = 3.1$, and thus contains much less light at large radii than an $R^{1/4}$-bulge. This difference illustrates once more the importance of using a general Sérsic profile for the bulge intensity distribution, rather than the less flexible de Vaucouleurs profile.

Although *UGC 12043* (NGC 7286) has the characteristic smooth light distribution of early-type disc galaxies, it completely lacks a central bulge component. The light profile shows only an exponential disc; the fitted exponential profiles are overplotted with the bold lines in the figure. This galaxy is also smaller and less luminous than other galaxies in our sample ($D^c_{25,R} = 7.8$ kpc, $M_R = -18.26$). This galaxy seems a member of a class of dwarf early-type spiral galaxies with distinctly different properties from their high-luminosity early-type counterparts (see also UGC 3580).

9 SUMMARY AND CONCLUSIONS

We have obtained deep *R*- and *B*-band surface photometry for a sample of 21 early-type disc galaxies with morphological types between S0 and Sab and *B*-band absolute magnitudes between -17 and -22. For six galaxies, *I*-band photometry is available as well. On average, our data reach surface brightness levels of 26.95, 26.07 and 24.26 mag arcsec^{-2} (3σ) in *B*, *R* and *I*, respectively.

For all galaxies, we have presented the results of our isophotal analysis, including radial variations of surface brightness, colour, ellipticity, position angle and deviations from axisymmetry. We have also determined isophotal and effective diameters and total magnitudes.

We have developed a new, interactive, bulge–disc decomposition method which takes into account the full 2D information from the images and decomposes them into spheroidal bulges with a general Sérsic intensity profile and discs with an arbitrary intensity distribution. We made no prior assumptions about the intrinsic axis ratios of the bulges, but rather determined those directly from the images by comparing the ellipticity of the bulge isophotes to that of the outer disc. We have shown that 1D bulge–disc decomposition methods, where analytic functions are fit directly to the radial photometric profiles, suffer from systematic biases, particularly in galaxies with large and luminous bulges. For example, they can lead to severe underestimates of the effective radii of the bulges. 2D techniques, which use the full information available in the image, are less affected by such biases and yield more accurate results on the structural parameters of the bulges.

From a comparison of different bulge and disc parameters, we find the following results concerning the structure of early-type disc galaxies.

(i) There is a wide range in BD luminosity and size ratios. The average value of $\log(L_b/L_d)$ is -0.23 ± 0.47 and the average ratio r_e/h is 0.32 ± 0.15 (excluding two galaxies, UGC 624 and 6786, which have unusually large bulges; see Section 8). The errors give the standard deviations of the samples. The common belief that early-type disc galaxies have large and luminous bulges does not hold in all cases; our sample contains several galaxies with faint and/or small bulges compared to the surrounding discs (e.g. UGC 94, 3205, 3546).

(ii) Luminous bulges have on average larger values for the Sérsic shape parameter *n*, consistent with previous studies. The average value for all bulges in our sample is $\langle n \rangle = 2.5 \pm 1.1$. Bulges of early-type disc galaxies form, at least as far as their *n* values is concerned, an intermediate population between elliptical galaxies and late-type galaxy bulges.

(iii) The three fundamental bulge parameters, μ_e, r_e and *n*, are all correlated with the large bulges having a lower effective surface brightness and a more strongly centrally peaked light distribution (higher *n*).

(iv) None of the galaxies in our sample harbours a truly spherical bulge; in contrast, several bulges are highly flattened with intrinsic axis ratios as low as 0.3–0.4 (e.g. UGC 5253, 9133). The average intrinsic axis ratio of the bulges in our sample is $\langle q_b \rangle = 0.55 \pm 0.12$. The flattening of the bulges is weakly coupled to their luminosity, more luminous bulges generally being more flattened than low-luminosity systems. The scatter in the relation is, however, large and more observations are needed to investigate this trend further.

(v) The fact that most bulges in our sample are significantly flattened and have an intensity profile shallower than $R^{1/4}$ suggests that many of the bulges in our sample are not miniature elliptical galaxies, but rather 'pseudo-bulges' formed from disc material by secular processes, in accordance with the ideas proposed by Kormendy & Kennicutt (2004). However, whereas they assumed that such pseudo-bulges occur mainly in later-type spiral galaxies, our results imply that they may be common in massive, early-type disc galaxies as well (cf. Laurikainen et al. 2006 and Erwin et al. 2003).

(vi) The single exception to the last point is UGC 6786. This galaxy is fully dominated by its bulge ($L_b/L_d = 3.91$, $r_e/h = 3.54$, all in *R*), which has a Sérsic *n* parameter of 5.5 and is almost spherical ($q_b = 0.8$). It has a clear disc component, but its luminosity profile is unusual, with a plateau of constant surface density in the centre and a steep exponential fall-off in the outer parts. It seems most logical to interpret this galaxy as an elliptical which has later acquired a disc of gas and stars (e.g. due to accretion or a merger event).

(vii) Many galaxies become bluer towards larger radii. In some cases, this can be explained solely by the radially declining contribution of the red bulge to the total light. In most cases, however, this effect is not sufficient and the discs themselves must contain colour gradients as well.

The results presented in this paper will be used in a future paper to calculate the contributions of the stellar components to the rotation curves of these early-type disc galaxies.

ACKNOWLEDGMENTS

EN is grateful to Alister W. Graham for helpful discussions about various issues related to bulge–disc decompositions, and for kindly providing the FORTRAN code to perform the least-squares fits to the bulge profiles. We would also like to thank Jelte de Jong for carrying out the observations of UGC 6786 and 7989 on the 2.4-m MDM Hiltner Telescope. We thank the referee, Phil James, for pointing out a few unclarities in the original version of the manuscript and for several suggestions for improvement.

REFERENCES

Andredakis Y. C., Sanders R. H., 1994, MNRAS, 267, 283
Andredakis Y. C., Peletier R. F., Balcells M., 1995, MNRAS, 275, 874
Baggett W. E., Baggett S. M., Anderson K. S. J., 1998, AJ, 116, 1626
Balcells M., Graham A. W., Domínguez-Palmero L., Peletier R. F., 2003, ApJ, 582, L79
Battinelli P., Capuzzo-Dolcetta R., Hodge P. W., Vicari A., Wyder T. K., 2000, A&A, 357, 437
Binney J., Tremaine S., 1987, Galactic Dynamics. Princeton Univ. Press, Princeton, NJ, p. 747
Buta R., van Driel W., Braine J., Combes F., Wakamatsu K., Sofue Y., Tomita A., 1995, ApJ, 450, 593
Byun Y. I., Freeman K. C., 1995, ApJ, 448, 563
Caon N., Capaccioli M., D'Onofrio M., 1993, MNRAS, 265, 1013
Carignan C., Freeman K. C., 1988, ApJ, 332, L33
Carollo C. M., 1999, ApJ, 523, 566
Carollo C. M., Stiavelli M., de Zeeuw P. T., Mack J., 1997, AJ, 114, 2366
Carollo C. M., Stiavelli M., Mack J., 1998, AJ, 116, 68
Côté S., Carignan C., Freeman K. C., 2000, AJ, 120, 3027
Courteau S., de Jong R. S., Broeils A. H., 1996, ApJ, 457, L73
de Blok W. J. G., McGaugh S. S., 1997, MNRAS, 290, 533
de Grijs R., 1998, MNRAS, 299, 595
de Jong R. S., 1996a, A&AS, 118, 557
de Jong R. S., 1996b, A&A, 313, 377
de Jong R. S., Simard L., Davies R. L., Saglia R. P., Burstein D., Colless M., McMahan R., Wegner G., 2004, MNRAS, 355, 1155
de Vaucouleurs G., 1948, Ann. Astrophys., 11, 247
de Vaucouleurs G., 1958, ApJ, 128, 465
de Vaucouleurs G., 1959, Handbuch der Physik, 53, 275
de Vaucouleurs G., 1961, ApJS, 5, 233
Emsellem E. et al., 2004, MNRAS, 352, 721
Erwin P., Sparke L. S., 1999, ApJ, 521, L37
Erwin P., Sparke L. S., 2002, AJ, 124, 65
Erwin P., Sparke L. S., 2003, ApJS, 146, 299
Erwin P., Beltrán J. C. V., Graham A. W., Beckman J. E., 2003, ApJ, 597, 929
Fathi K., 2004, PhD thesis, Rijksuniversiteit Groningen
Freeman K. C., 1970, ApJ, 160, 811
González Delgado R. M., Perez E., Tadhunter C., Vilchez J. M., Rodriguez-Espinosa J. M., 1997, ApJS, 108, 155
Graham A. W., 2001, AJ, 121, 820
Huchra J. P., Wyatt W. F., Davis M., 1982, AJ, 87, 1628
Hunt L. K., Pierini D., Giovanardi C., 2004, A&A, 414, 905
Illingworth G., Schechter P. L., 1982, ApJ, 256, 481
James P. A. et al., 2004, A&A, 414, 23
Jedrzejewski R. I., 1987, MNRAS, 226, 747
Jerjen H., Binggeli B., Freeman K. C., 2000, AJ, 119, 593
Kamphuis J. J., Sijbring D., van Albada T. S., 1996, A&AS, 116, 15
Kennicutt R. C., 1989, ApJ, 344, 685
Khosroshahi H. G., Wadadekar Y., Kembhavi A., 2000, ApJ, 533, 162
Kormendy J., 1993, in IAU Symposium 153: Galactic Bulges Kinematics of Extragalactic Bulges: Evidence that Some Bulges are Really Discs. Kluwer, Dordrecht, p. 209
Kormendy J., Illingworth G., 1982, ApJ, 256, 460
Kormendy J., Kennicutt R. C., 2004, ARA&A, 42, 603
Landolt A. U., 1992, AJ, 104, 340
Laurikainen E., Salo H., Buta R., 2005, MNRAS, 362, 1319
Laurikainen E., Salo H., Buta R., Knapen J., Speltincx T., Block D., 2006, AJ, 132, 2634
MacArthur L. A., Courteau S., Holtzman J. A., 2003, ApJ, 582, 689
Matthews L. D., Gallagher J. S., van Driel W., 1999, AJ, 118, 2751
Möllenhoff C., Popescu C. C., Tuffs R. J., 2006, A&A, 456, 941
Morganti R. et al., 2006, MNRAS, 371, 157
Nagar N. M., Wilson A. S., Mulchaey J. S., Gallimore J. F., 1999, ApJS, 120, 209
Noordermeer E., van der Hulst J. M., Sancisi R., Swaters R. A., van Albada T. S., 2005, A&A, 442, 137 (Paper I)
Noordermeer E., van der Hulst J. M., Sancisi R., Swaters R. A., van Albada T. S., 2007, MNRAS, in press (doi:10.1111/j.1365-2966.2007.11533.x) (this issue)
Oosterloo T. A., Morganti R., Sadler E. M., Vergani D., Caldwell N., 2002, AJ, 123, 729
Palunas P., Williams T. B., 2000, AJ, 120, 2884
Pogge R. W., 1989, ApJS, 71, 433
Rix H.-W., White S. D. M., 1990, ApJ, 362, 52
Roberts M. S., Haynes M. P., 1994, ARA&A, 32, 115
Russell J. L., Lasker B. M., McLean B. J., Sturch C. R., Jenkner H., 1990, AJ, 99, 2059
Schlegel D. J., Finkbeiner D. P., Davis M., 1998, ApJ, 500, 525
Scorza C., Bender R., 1995, A&A, 293, 20
Sérsic J. L., 1968, Atlas de Galaxias Australes. Observatorio Astronomico, Cordoba, Argentina
Swaters R., 1999, PhD thesis, Rijksuniversiteit Groningen
Trujillo I., Aguerri J. A. L., Cepa J., Gutiérrez C. M., 2001a, MNRAS, 321, 269
Trujillo I., Graham A. W., Caon N., 2001b, MNRAS, 326, 869
Ulvestad J. S., Wilson A. S., 1984, ApJ, 285, 439
van der Hulst J. M., van Albada T. S., Sancisi R., 2001, ASP Conf. Ser. Vol. 240, Gas and Galaxy Evolution The Westerbork H I Survey of Irregular and Spiral Galaxies, WHISP. Astron. Soc. Pac., San Francisco, p. 451
van der Kruit P. C., 1979, A&AS, 38, 15
van Driel W., Buta R. J., 1991, A&A, 245, 7
Verdes-Montenegro L., Bosma A., Athanassoula E., 1995, A&A, 300, 65
Véron-Cetty M.-P., Véron P., 1996, A&AS, 115, 97
Young C. K., Currie M. J., 1994, MNRAS, 268, L11
Zwicky F., Zwicky M. A., 1971, Catalogue of Selected Compact Galaxies and of Post-Eruptive Galaxies. Zwicky, Guemligen

APPENDIX A: TABLES

Table A1. List of observations. (1) Galaxy name; (2) colour band; (3) telescope used; (4) observing dates; (5) total exposure time; (6) effective seeing; (7) photometric error and (8) magnitude corresponding to $3\sigma_{bg}$ above sky level (see text for detailed description of the columns).

UGC	Band	Telescope	Dates	t_{exp} (s)	Seeing (arcsec)	σ_{phot} (mag)	$\mu_{3\sigma}$ (mag)
(1)	(2)	(3)	(4)	(5)	(6)	(7)	(8)
89	*R*	JKT	2000/11/2[b], 2000/11/4	2800	1.1	0.076	26.12
	B	JKT	2000/11/4	2400	1.3	0.12	26.63
94	*R*	INT	2000/11/5	600	1.5	0.038	25.77
	B	INT	2000/11/5	600	1.7	0.029	27.77
624	*R*	JKT	2000/10/31	2400	0.8	0.049	26.71
	B	INT	2000/11/5	600	1.8	0.030	28.64
	I	JKT	2001/1/27	1440	1.3	0.049	24.19
1541	*R*	JKT	2000/11/2[b], 2000/11/3	2880	1.6	0.093	26.23
	B	JKT	2000/11/3	2400	2.2	0.16	27.72
	I	JKT	2001/1/27	1500	1.4	0.047	24.48
2487	*R*	JKT	2000/10/29, 2000/10/30	2400	1.8	0.027	26.36
	B	JKT	2001/1/24	2400	1.3	0.072	26.46
2916	*R*	JKT	2000/10/31	2400	1.0	0.056	26.80
	B	JKT	2000/11/5	2400	1.8	0.019	27.38
2953	*R*[a]	JKT	2001/11/18[b]	2400	1.7	0.029[c]	24.83
	R[a]	INT	1995/2/3[b]	180	2.2	0.51[c]	26.83
	B[a]	JKT	2000/11/4, 2000/11/5	3300	1.9	0.14	25.47
	B[a]	JKT	2001/11/18[b]	2400	2.1	0.055[c]	25.43
	I	JKT	2001/1/29	1800	1.1	0.15	23.05
3205	*R*[a]	JKT	2001/1/26	1800	1.3	0.12	25.59
	R[a]	JKT	2000/10/29	2400	3.6	0.032	25.22
	B	JKT	2000/11/1	2400	1.0	0.17	26.68
	I	JKT	2001/1/30	2000	3.1	0.20	23.92
3546	*R*[a]	JKT	2000/10/30	2400	0.9	0.028	26.27
	R[a]	JKT	2001/1/26	1800	1.2	0.13	26.03
	R[a]	JKT	2001/11/18[b]	2400	2.0	0.028[c]	26.79
	B[a]	JKT	2000/10/30, 2000/11/5	2400	1.6	0.22	27.77
	B[a]	JKT	2001/11/18[b]	2400	2.0	0.052[c]	27.09
3580	*R*	INT	1995/27/12	300	1.0	0.051	26.20
	B	INT	1995/27/12	300	1.2	0.12	28.05
3993	*R*	JKT	2001/1/26	2400	1.2	0.16	26.86
	B	JKT	2002/4/2[d]	500	1.7	0.18	25.74
4458	*R*	JKT	2000/11/2[b], 2000/11/3	3680	1.1	0.095	26.56
	B[a]	JKT	2001/1/25	2400	2.0	0.18	27.15
	B[a]	JKT	2000/11/3	2400	2.1	0.15	26.32
5253	*R*	INT	1994/5/3	300	1.6	0.24	26.84
	B	JKT	2002/4/4[b,d]	1800	1.6	0.14[c]	26.19
6786	*R*[a]	JKT	2001/1/31	720	1.1	0.053	25.69
	R[a]	MDM	2003/1/1	480	1.4	0.022	25.63
6787	*R*	JKT	2000/5/29	1800	1.7	0.26	26.41
	B	JKT	2001/1/31	1800	1.2	0.11	27.82
8699	*R*	JKT	2000/5/24	2400	1.6	0.24	25.33
	B	JKT	2000/5/24	2400	1.7	0.11	25.76
9133	*R*	JKT	2000/5/26, 2000/5/27	2400	1.3	0.086	25.61
	B	JKT	2000/6/1, 2002/4/19[d]	3000	2.3	0.085	27.23
11670	*R*	JKT	2000/5/26	3000	1.3	0.11	25.98
	B	JKT	2000/5/30[b]	2400	1.3	0.19[c]	27.01
	I	JKT	2000/5/31[b], 2000/6/1	2400	1.1	0.14	25.12
11852	*R*	JKT	2000/5/27	2400	0.9	0.081	25.86
	B	JKT	2000/5/27	2400	1.1	0.084	26.58
	I	JKT	2000/6/1	2400	1.1	0.075	24.82
11914	*R*	JKT	2000/5/30[b], 2000/5/31[b], 2002/6/3[d]	2900	1.1	0.22	25.40
	B	JKT	2000/5/30[b], 2002/6/3[d]	2900	1.3	0.24	26.65
12043	*R*	JKT	2000/5/29	2400	1.2	0.26	26.04
	B	JKT	2000/5/31[b], 2001/6/1	3300	1.4	0.12	26.37

[a]Multiple exposures used to check consistency of our observations (see Section 5). Only the first observation listed for each band is used in the remainder of this paper.
[b]Night with non-photometric conditions.
[c]Lower limit for photometric error only due to non-photometric conditions during observations.
[d]Observations done in service mode at the JKT.
[e]Mosaic of four pointings.

Table A2. Isophotal properties: (1) UGC number; (2) RA and (3) Dec. of central position; (4) uncertainty in central position and (5) dominant source of uncertainty; (6) position angle (north through east) of major axis; (7) ellipticity and (8) inclination angle.

UGC	Central position						Uncertainty		PA	ϵ	i
	RA (2000)			Dec. (2000)			$\sigma_{\rm pos}$	Source			
	h	m	s	$^\circ$	$'$	$''$	(arcsec)		($^\circ$)		($^\circ$)
(1)	(2)			(3)			(4)	(5)	(6)	(7)	(8)
89	0	9	53.47	25	55	26.0	0.6	DSS	−14	0.37	52
94	0	10	26.05	25	49	47.5	0.6	DSS	−76	0.34	50
624	1	0	36.42	30	40	8.6	0.6	DSS	−72	0.52	64
1541	2	3	27.97	38	7	0.9	0.6	DSS	67	0.26	43
2487	3	1	42.34	35	12	20.6	0.6	DSS	70	0.20	38
2916	4	2	33.8	71	42	21.1	0.6	DSS	53	0.14	31
2953	4	7	46.7	69	48	46.7	0.6	DSS	−85	0.33	49
3205	4	56	14.88	30	3	8.3	0.6	DSS	42	0.60	69
3546	6	50	8.7	60	50	45.4	0.6	DSS	51	0.37	52
3580	6	55	30.9	69	33	47.1	1.0	Dust	7	0.48	61
3993	7	55	44.1	84	55	35.4	0.6	DSS	44	0.08	23
4458	8	32	11.34	22	33	38.3	0.6	DSS	−72	0.12	29
5253	9	50	22.50	72	16	44.3	0.6	DSS	−3	0.18	36
6786	11	49	9.52	27	1	20.2	0.6	DSS	1	0.45	58[a]
6787	11	49	15.26	56	5	5.5	0.6	DSS	−73	0.40	55[a]
8699	13	45	8.74	41	30	12.3	0.6	DSS	−81	0.70	77
9133	14	16	7.76	35	20	38.3	0.6	DSS	26	0.37	52
11670	21	3	33.56	29	53	51.2	0.6	DSS	−26	0.58	68
11852	21	55	59.27	27	53	55.6	0.6	DSS	13	0.38	53
11914	22	7	52.43	31	21	34.5	0.6	DSS	81	0.10	26
12043	22	27	50.53	29	5	45.9	0.7	DSS	−84	0.60	69

[a]Isophotes not representative of disc ellipticity (see text).

Table A3. Photometric properties: (1) UGC number; (2) colour band for Columns (3) to (14); (3) and (4) raw isophotal diameters at 25 and 26.5 mag arcsec^{-2}; (5) and (6) idem, but corrected for inclination and Galactic foreground extinction; (7)–(9) effective radii containing 20, 50 and 80 per cent of the total light; (10) conversion factor to convert arcsec into kpc; (11) and (12) total apparent magnitudes within the 25th mag arcsec^{-2} diameter and within the last measured point; (13) and (14) total absolute magnitudes (corrected for Galactic foreground extinction).

UGC	Band	D_{25} (arcsec)	$D_{26.5}$ (arcsec)	D^c_{25} (arcsec)	$D^c_{26.5}$ (arcsec)	R_{20} (arcsec)	R_{50} (arcsec)	R_{80} (arcsec)	Scale (kpc arcsec^{-1})	m_{25} (mag)	$m_{\rm lim}$ (mag)	M_{25} (mag)	$m_{\rm lim}$ (mag)
(1)	(2)	(3)	(4)	(5)	(6)	(7)	(8)	(9)	(10)	(11)	(12)	(13)	(14)
89	*R*	197	–	181	237	4.4	23	40	0.30	11.41 ± 0.08	11.38 ± 0.08	−22.66	−22.69
	B	145	202	129	191	4.2	23	40	0.30	12.76 ± 0.12	12.68 ± 0.13	−21.37	−21.45
94	*R*	107	–	98	136	9.8	12	28	0.30	12.72 ± 0.04	12.69 ± 0.04	−21.36	−21.39
	B	87	121	82	107	9.9	15	31	0.30	13.92 ± 0.03	13.83 ± 0.03	−20.23	−20.32
624	*R*	192	258	145	225	5.3	18	42	0.32	11.98 ± 0.05	11.96 ± 0.05	−22.23	−22.25
	B	112	191	91	149	6.6	20	42	0.32	13.61 ± 0.03	13.48 ± 0.03	−20.70	−20.83
	I	–	–	166	–	5.0	16	37	0.32	–	11.23 ± 0.07	–	−22.94
1541	*R*	145	–	137	–	4.0	19	39	0.37	12.21 ± 0.09	12.17 ± 0.09	−22.37	−22.41
	B	106	167	104	163	5.3	27	44	0.37	13.73 ± 0.16	13.55 ± 0.16	−20.94	−21.12
	I	–	–	–	–	3.9	16	37	0.37	–	11.47 ± 0.05	–	−23.07
2487	*R*	211	275	220	–	9.3	30	63	0.33	11.43 ± 0.03	11.39 ± 0.03	−23.20	−23.24
	B	143	217	166	–	9.8	32	68	0.33	13.27 ± 0.08	13.06 ± 0.10	−21.67	−21.88
2916	*R*	113	148	125	–	5.0	14	33	0.31	12.80 ± 0.06	12.75 ± 0.06	−21.96	−22.01
	B	80	118	106	–	6.3	17	35	0.31	14.34 ± 0.02	14.18 ± 0.03	−20.89	−21.05
2953	*R*	531[a]	–	–	–	32	81	150	0.073	9.49 ± 0.05[a]	9.48 ± 0.05[a]	−22.53	−22.54
	B	338	–	–	–	32	77	133	0.073	11.56 ± 0.15	11.49 ± 0.16	−21.15	−21.22
	I	–	–	–	–	31	76	144	0.073	–	8.34 ± 0.16	–	−23.37
3205	*R*	142	–	148	–	9.9	23	40	0.24	13.02 ± 0.12	13.00 ± 0.12	−21.86	−21.88
	B	90	146	138	–	12	27	47	0.24	15.15 ± 0.17	14.88 ± 0.18	−20.62	−20.89
	I	–	–	–	–	11	24	43	0.24	–	12.01 ± 0.21	–	−22.48
3546	*R*	234	–	224	270	8.9	25	66	0.13	11.03 ± 0.03	11.02 ± 0.03	−21.34	−21.35
	B	193	236	185	230	11	28	70	0.13	12.54 ± 0.22	12.47 ± 0.22	−19.95	−20.02
3580	*R*	196	253	164	231	8.9	25	58	0.093	12.18 ± 0.04	12.14 ± 0.05	−19.38	−19.42
	B	140	215	111	189	8.6	26	62	0.093	13.52 ± 0.01	13.33 ± 0.02	−18.12	−18.31
3993	*R*	106	135	108	137	3.5	11	28	0.30	12.82 ± 0.16	12.78 ± 0.16	−21.31	−21.35
	B	88	–	92	–	4.4	14	36	0.30	14.18 ± 0.19	14.04 ± 0.20	−20.05	−20.19
4458	*R*	188	272	186	270	4.5	19	56	0.31	11.58 ± 0.10	11.52 ± 0.10	−22.55	−22.61
	B	134	222	134	222	5.6	25	67	0.31	13.05 ± 0.18	12.81 ± 0.18	−21.14	−21.38
5253	*R*	433	–	417	543	12	42	103	0.10	9.81 ± 0.24	9.79 ± 0.24	−21.88	−21.90
	B	354[a]	–	333[a]	490[a]	17	55	123	0.10	10.97 ± 0.14[$]	10.88 ± 0.15[a]	−20.77	−20.86
6786	*R*	262	–	224	323	9.6	29	64	0.13	11.05 ± 0.05	11.02 ± 0.06	−21.10	−21.13
6787	*R*	316	–	288	365	7.4	29	75	0.092	10.17 ± 0.26	10.16 ± 0.26	−21.27	−21.28
	B	260	383	223	340	9.5	37	90	0.092	11.57 ± 0.11	11.47 ± 0.11	−19.90	−20.00
8699	*R*	184	–	118	179	5.8	18	42	0.18	12.14 ± 0.24	12.11 ± 0.24	−20.71	−20.74
	B	137	–	93	133	6.7	21	43	0.18	13.45 ± 0.11	13.39 ± 0.11	−19.42	−19.48
9133	*R*	276	–	244	336	8.6	31	77	0.26	11.13 ± 0.09	11.09 ± 0.09	−22.58	−22.62
	B	190	274	159	251	11	36	78	0.26	12.66 ± 0.09	12.52 ± 0.09	−21.08	−21.22
11670	*R*	306	–	282	365	12	34	76	0.062	10.57 ± 0.11	10.55 ± 0.11	−20.53	−20.55
	B	224[a]	305[a]	218[a]	299[a]	14	36	79	0.062	12.33 ± 0.19[a]	12.25 ± 0.19[a]	−19.12	−19.20
	I	367	–	333	–	13	37	81	0.062	9.82 ± 0.14	9.81 ± 0.14	−21.12	−21.13
11852	*R*	101	–	93	–	4.8	13	29	0.39	13.20 ± 0.08	13.17 ± 0.08	−21.50	−21.53
	B	81	121	76	112	6.4	16	37	0.39	14.57 ± 0.09	14.38 ± 0.10	−20.25	−20.44
	I	–	–	122	–	5.7	16	37	0.39	–	12.51 ± 0.09	–	−22.14
11914	*R*	367	–	374	–	16	45	91	0.072	9.77 ± 0.22	9.75 ± 0.22	−21.33	−21.35
	B	251	342	266	356	16	42	81	0.072	11.04 ± 0.24	10.98 ± 0.24	−20.21	−20.27
12043	*R*	129	–	104	143	8.3	18	34	0.075	12.88 ± 0.26	12.85 ± 0.26	−18.23	−18.26
	B	109	154	89	128	8.3	18	35	0.075	13.75 ± 0.12	13.68 ± 0.12	−17.46	−17.53

[a]Values from non-photometric data. Isophotal diameters uncertain; errors on magnitudes are lower limits only.

Table A4. Results from the bulge–disc decompositions: (1) UGC number; (2) colour band for Columns (3) to (17); (3) conversion factor to convert arcsec into kpc; (4) bulge ellipticity; (5) bulge intrinsic axis ratio; (6) bulge effective surface brightness; (7) idem, but corrected for Galactic foreground extinction; (8) bulge effective radius; (9) bulge Sérsic parameter, (10) bulge total apparent magnitude; (11) bulge total absolute magnitude (corrected for Galactic foreground extinction); (12) disc central surface brightness; (13) idem, but corrected for inclination and Galactic foreground extinction; (14) disc scalelength; (15) disc total apparent magnitude; (16) disc total absolute magnitude (corrected for Galactic foreground extinction) and (17) total BD luminosity ratio.

UGC	Band	Scale	Bulge parameters								Disc parameters					
			ϵ_b	q_b	μ_e	μ_e^c	r_e	n	m_b	M_b	μ_0	μ_0^c	h	m_d	M_d	B/D
		(kpc arcsec^{-1})			(mag arcsec^{-2})	(mag arcsec^{-2})	(arcsec)		(mag)	(mag)	(mag arcsec^{-2})	(mag arcsec^{-2})	(arcsec)	(mag)	(mag)	
(1)	(2)	(3)	(4)	(5)	(6)	(7)	(8)	(9)	(10)	(11)	(12)	(13)	(14)	(15)	(16)	(17)
89	*R*	0.30	0.25	0.5	17.53	17.43	2.9	1.2	12.77	−21.30	20.19	20.61	22.1	11.75	−22.32	0.39
	B	0.30	Idem		18.84	18.67	Idem		14.08	−20.05	21.29	21.65	21.2	13.05	−21.08	0.39
94	*R*	0.30	0.14	0.7	21.43	21.33	3.7	2.5	15.58	−18.50	20.04	20.42	11.9	13.00	−21.08	0.09
	B	0.30	Idem		23.24	23.08	Idem		17.41	−16.74	21.02	21.33	12.0	14.01	−20.14	0.04
624	*R*	0.32	0.33	0.5	21.10	20.95	15.0	3.7	12.30	−21.91	21.17	21.92	18.3	13.34	−20.87	2.60
	B	0.32	Idem		22.94	22.70	Idem		14.19	−20.12	21.87	22.53	17.7	14.34	−19.97	1.15
	I	0.32	Idem		20.52	20.41	Idem		11.82	−22.35	19.00	19.79	12.9	12.26	−21.91	1.50
1541	*R*	0.37	0.16	0.6	19.10	18.95	4.2	2.2	13.09	−21.49	20.84	21.03	19.6	12.73	−21.85	0.72
	B	0.37	Idem		20.78	20.54	Idem		14.77	−19.90	22.26	22.36	21.5	13.92	−20.75	0.46
	I	0.37	Idem		18.40	18.29	Idem		12.39	−22.15	19.91	20.14	18.1	12.02	−22.52	0.71
2487	*R*	0.33	0.11	0.7	19.89	19.40	6.7	1.7	12.94	−21.69	20.35	20.12	24.4	11.69	−22.94	0.32
	B	0.33	Idem		21.52	20.73	Idem		14.57	−20.37	22.24	21.71	27.5	13.40	−21.54	0.34
2916	*R*	0.31	0.12[a]	0.4[a]	21.09	20.34	8.8	2.3	13.40	−21.36	21.57	20.99	16.1	13.60	−21.16	1.20
	B	0.31	Idem		22.97	21.76	Idem		15.26	−19.97	22.31	21.27	14.6	14.68	−20.55	0.59
2953	*R*	0.073	0.20	0.6	21.34[c]	20.22[c]	24.1	3.3	11.38[c]	−20.64[c]	19.92[c]	19.25[c]	56.1	9.69[c]	−22.33[c]	0.21
	B	0.073	Idem		23.60	21.78	Idem		13.68	−19.03	21.72	20.36	53.8	11.68	−21.03	0.16
	I	0.073	Idem		20.19	19.37	Idem		10.26	−21.45	18.68	18.32	54.1	8.58	−23.13	0.21
3205	*R*	0.24	0.24[b]	0.7[b]	20.06	18.61	2.2	0.8[b]	16.03	−18.85	19.92	19.59	14.8	13.08	−21.80	0.07
	B	0.24	Idem		22.13	19.80	Idem		18.12	−17.65	22.19	20.97	18.2	14.94	−20.83	0.05
	I	0.24	Idem		19.65	18.60	Idem		15.78	−18.71	18.97	19.04	15.7	12.04	−22.45	0.03
3546	*R*	0.13	0.22	0.6	17.48	17.29	2.2	1.0	13.40	−18.97	19.15	19.49	21.1	11.13	−21.24	0.12
	B	0.13	Idem		19.14	18.84	Idem		15.07	−17.42	20.71	20.93	22.0	12.56	−19.93	0.10
3580	*R*	0.093	0.28	0.6	20.22	20.08	8.0	1.4	13.22	−18.34	20.93	21.58	25.5	12.65	−18.91	0.59
	B	0.093	Idem		21.36	21.13	Idem		14.37	−17.27	22.25	22.81	26.7	13.87	−17.77	0.63
3993	*R*	0.30	0.05[d]	0.5[d]	20.53	20.36	7.1	2.7	13.16	−20.97	22.45	22.37	18.2	14.07	−20.06	2.32
	B	0.30	Idem		22.03	21.76	Idem		14.69	−19.54	23.42	23.23	24.0	14.91	−19.32	1.23
4458	*R*	0.31	0.10	0.4	19.21	19.12	5.8	2.6	12.32	−21.81	21.21	21.26	27.7	12.21	−21.92	0.91
	B	0.31	Idem		20.72	20.57	Idem		13.82	−20.37	22.62	22.62	31.3	13.35	−20.84	0.65
5253	*R*	0.10	0.15	0.4	20.48	20.41	25.1	3.9	10.28	−21.41	21.16	21.32	52.2	10.80	−20.89	1.62
	B	0.10	Idem		21.98[c]	21.86[c]	Idem		11.82[c]	−19.92[c]	21.95[c]	22.06[c]	57.6	11.43[c]	−20.31[c]	0.70
6786	*R*	0.13	0.21	0.8[f]	22.43	22.35	43.5	5.5	11.18	−20.97	18.27[e]	19.30[e]	12.3[e]	12.66	−19.49	3.91
6787	*R*	0.092	0.38	0.4[g]	18.43	18.37	8.8	2.3	11.13	−20.31	19.76	20.49	36.2	10.70	−20.74	0.68
	B	0.092	Idem		19.89	19.80	Idem		12.59	−18.88	21.30	22.00	42.9	11.92	−19.55	0.54
8699	*R*	0.18	0.40	0.6	19.58	19.55	6.9	2.7	12.77	−20.08	20.65	22.24	20.8	13.14	−19.71	1.41
	B	0.18	Idem		21.14	21.10	Idem		14.29	−18.58	21.81	23.39	21.0	14.13	−18.74	0.86

Table A4 – *continued*

UGC	Band	Scale	Bulge parameters								Disc parameters					B/D
		(kpc arcsec^{-1})	ϵ_b	q_b	μ_e (mag arcsec^{-2})	μ_e^c (mag arcsec^{-2})	r_e (arcsec)	n	m_b (mag)	M_b (mag)	μ_0 (mag arcsec^{-2})	μ_0^c (mag arcsec^{-2})	h (arcsec)	m_d (mag)	M_d (mag)	
(1)	(2)	(3)	(4)	(5)	(6)	(7)	(8)	(9)	(10)	(11)	(12)	(13)	(14)	(15)	(16)	(17)
9133	*R*	0.26	0.32	0.3	19.79	19.75	9.9	2.7	12.05	−21.66	20.78	21.27	34.4	11.69	−22.02	0.72
	B	0.26	Idem		21.52	21.45	Idem		13.78	−19.96	21.93	22.39	32.4	12.93	−20.81	0.46
11670	*R*	0.062	0.30	0.6	18.58	18.00	5.8	1.6	12.20	−18.90	19.09	19.58	28.5	10.83	−20.27	0.28
	B	0.062	Idem		20.76[c]	19.83[c]	Idem		14.39[c]	−17.06[c]	20.69[c]	20.82[c]	28.3	12.42[c]	−19.03[c]	0.16
	I	0.062	Idem		17.90	17.48	Idem		11.53	−19.41	18.50	19.15	30.8	10.05	−20.89	0.26
11852	*R*	0.39	0.25	0.6	20.55	20.36	5.1	2.2	14.27	−20.43	20.37	20.74	11.6	13.66	−21.04	0.57
	B	0.39	Idem		22.06	21.76	Idem		15.78	−19.04	22.04	22.29	15.3	14.73	−20.09	0.38
	I	0.39	Idem		19.98	19.84	Idem		14.17	−20.48	20.27	20.69	15.8	12.77	−21.88	0.28
11914	*R*	0.072	0.08	0.5	20.90	20.66	26.2	3.1	10.63	−20.47	20.03	19.91	36.8	10.38	−20.72	0.80
	B	0.072	Idem		22.29	21.91	Idem		12.06	−19.19	20.74	20.48	29.9	11.47	−19.78	0.58
12043	*R*	0.075	No bulge component present in this galaxy								18.96	19.90	11.3	12.85	−18.26	–
	B	0.075									19.84	20.68	11.5	13.68	−17.53	–

[a] Galaxy with nuclear bar. Ellipticity of bulge isophotes does not converge to constant value; average value is ad hoc estimate only.
[b] Value poorly constrained due to small size of bulge (see text).
[c] Values from non-photometric data.
[d] Values poorly constrained due to small inclination angle of galaxy (see text).
[e] Not a regular exponential disc (see text).
[f] Bulge axis ratio calculated using inclination angle of 69° (see text).
[g] Bulge axis ratio calculated using inclination angle of 61° (see text).

APPENDIX B: ATLAS OF IMAGES AND PHOTOMETRIC RESULTS

On the following pages, we present the results of the photometric analysis and bulge–disc decompositions. For all galaxies, we show on the first row three columns with photometric data:

Left-hand column

R-band image. Grey-scales are logarithmic in intensity. The cross denotes the centre; its coordinates are given in Table A2. A bar indicating the physical size of the galaxy is shown in the top left of the panel.

Middle column

Top panel. Photometric profiles in the available bands. Crosses, squares and triangles indicate the *I*, *R* and *B* band, respectively. The error bars on the symbols in the top right corner show the photometric errors $\sigma_{\rm phot}$, which are listed in Table A1.

Bottom panel. Colour profiles. Only points with error smaller than 0.5 mag are shown.

Right-hand column

Orientation and deviations from axisymmetry. All data in this column are measured from the *R*-band images. From *top* to *bottom*:

(i) Position angle (north through east): the data points with error bars give the results from an ellipse fit to the image with position angle and ellipticity as free parameters. The dashed line gives the adopted value which was used to derive the photometric profiles in the middle column. It is listed in Table A2.

(ii) Ellipticity: symbols and dashed line as for the position angle above.

(iii) Lopsidedness: data points show the amplitude of the $m = 1$ Fourier term of the intensity distribution measured along the ellipses, relative to the average intensity at the ellipse.

(iv) Phase of the $m = 1$ Fourier term: data points show the position angle, measured north through east, where the $m = 1$ Fourier term reaches maximum intensity.

(v) Bar strength or oval distortion: same as the third panel, but for the $m = 2$ Fourier term.

(vi) Phase of the $m = 2$ Fourier term: same as the fifth panel, but for one of the maxima of the $m = 2$ Fourier term.

The four columns in the second row contain the following results from the bulge–disc decompositions:

First column:

Model *R*-band image of the bulge; the grey-scale used is the same as in the original image shown in the first row.

Second column:

Top panel: bulge photometric profiles. Symbols show the photometric profiles measured from the images with an initial estimate for the disc subtracted. Only points within the bulge–disc transition radius are shown. The solid lines show the fitted Sérsic profiles; the fitted parameters are given in Table A4 and were used to create the model images shown in the first column (see Section 6.1 for details).

Bottom panel: bulge colour profiles. Only the colours of the fitted profiles are shown; since we used the same effective radius and Sérsic shape parameter for the fits in all bands, no colour gradients are fitted, and only a global colour is derived for the bulges.

Third column:

Residual *R*-band image after subtraction of the bulge component; the grey-scale used is the same as in the original image shown in the first row. Black marks indicate regions in the original image which were masked in an earlier stage of the reduction process (Section 3). All light in this image is assumed to originate from a flat disc component.

Fourth column:

Top panel: disc photometric profiles. Symbols show the profiles measured from the bulge-subtracted images. Only points outside the bulge–disc transition radius are shown. The solid lines show the fitted exponential profiles; the fitted parameters are given in Table A4 (see Section 6.2 for details).

Bottom panel: disc colour profiles. Only points with error smaller than 0.5 mag are shown.

UGC 12043 does not have a distinctive bulge component, so no bulge–disc decomposition was made and all light was assumed to originate from a flattened disc (see note in Section 8). For this galaxy, we show only the three columns with photometric data. The fitted exponential profiles for this galaxy are overplotted with the bold lines over the photometric profiles in the top panel of the middle column.

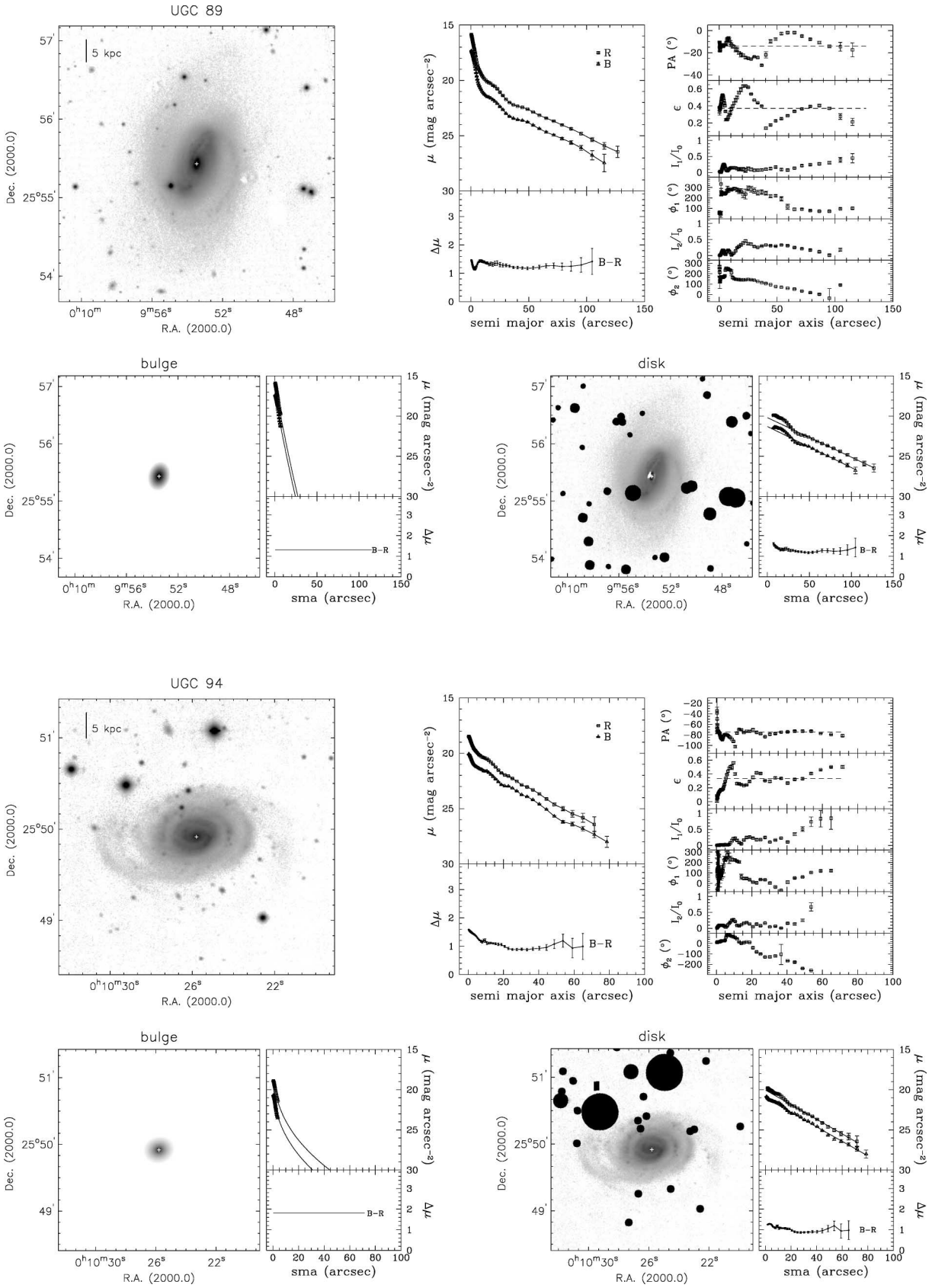

Figure B1. The results of the photometric analysis and bulge–disc decompositions.

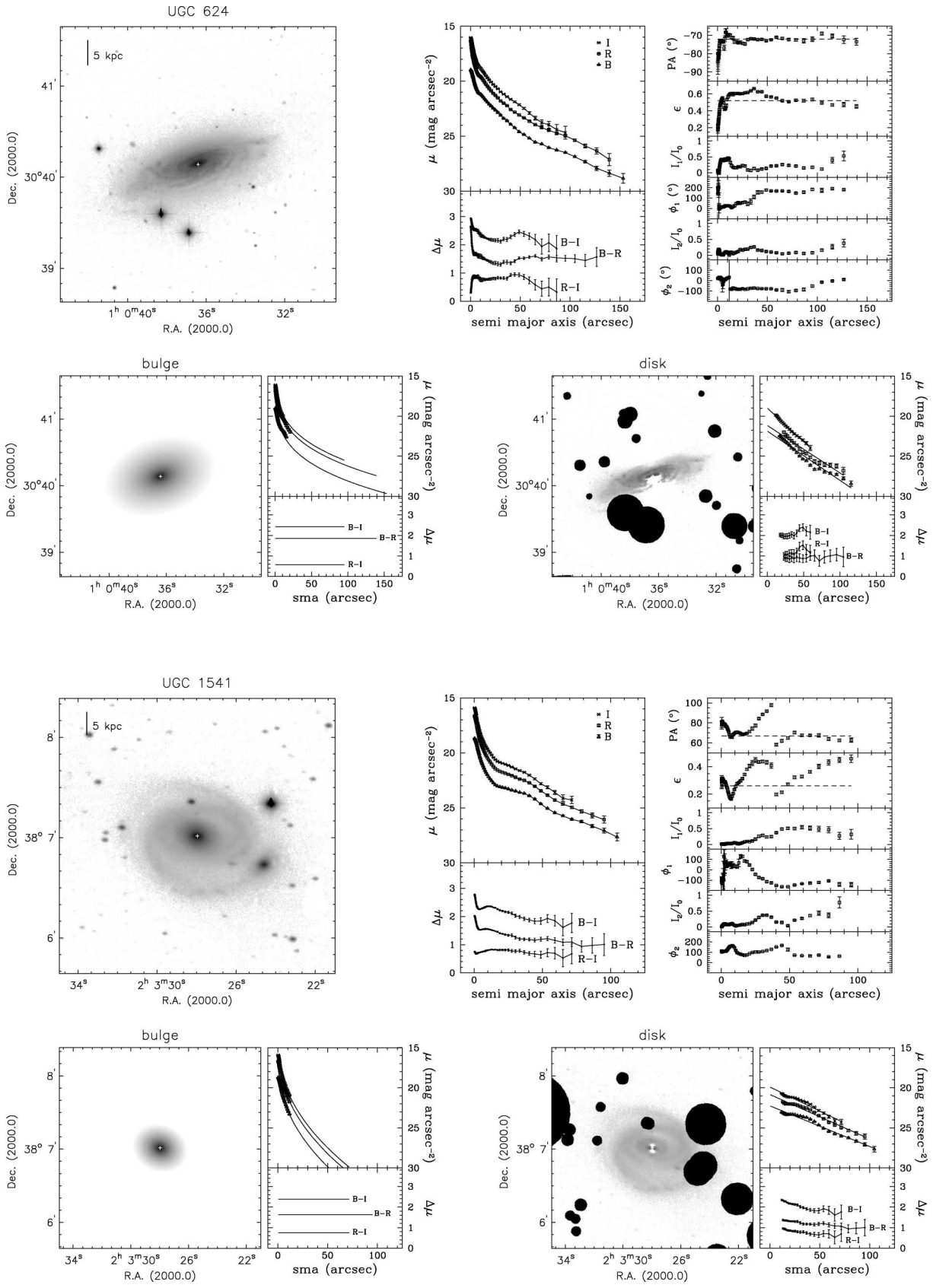

Figure B1 – *continued*

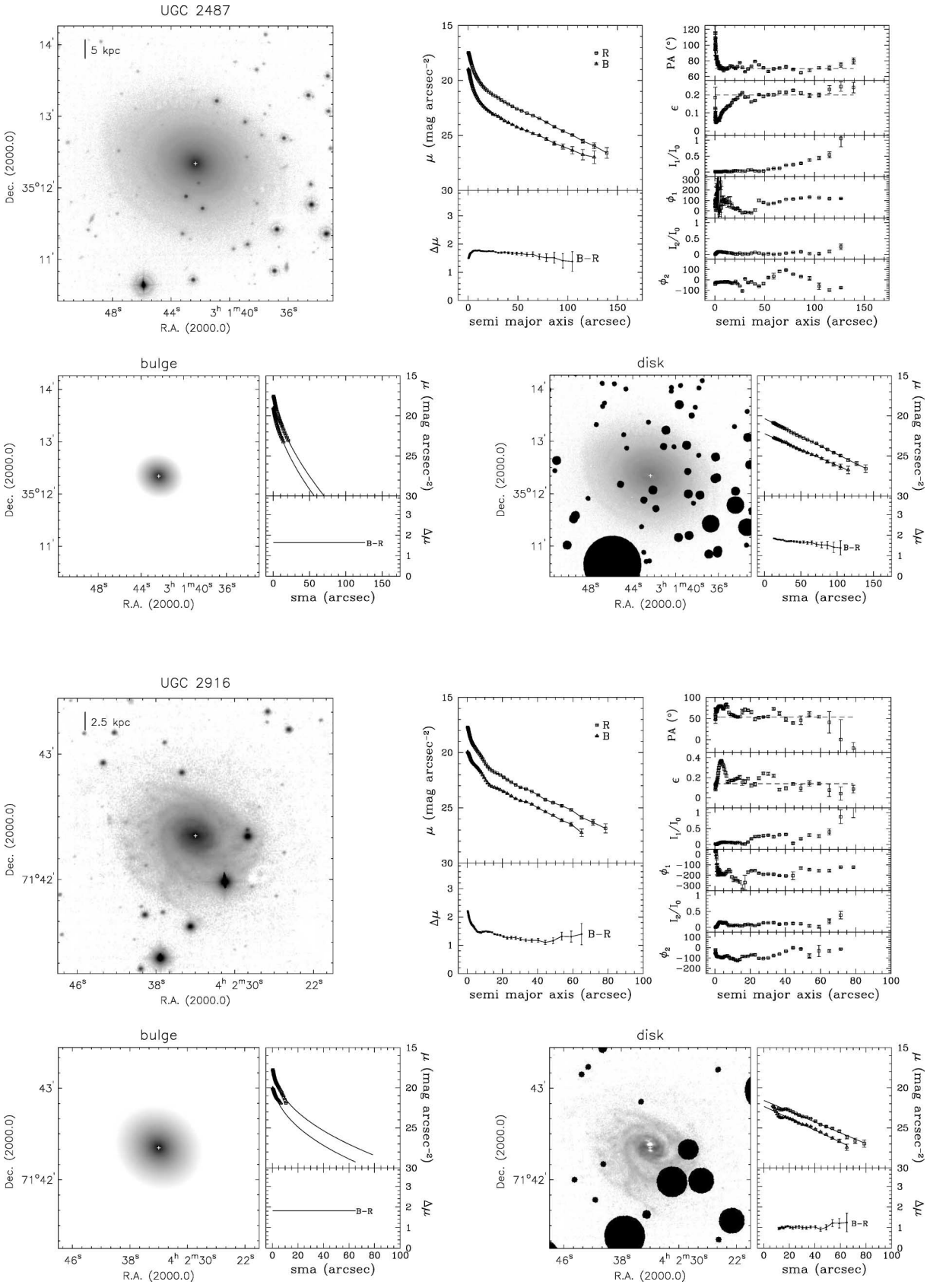

Figure B1 – *continued*

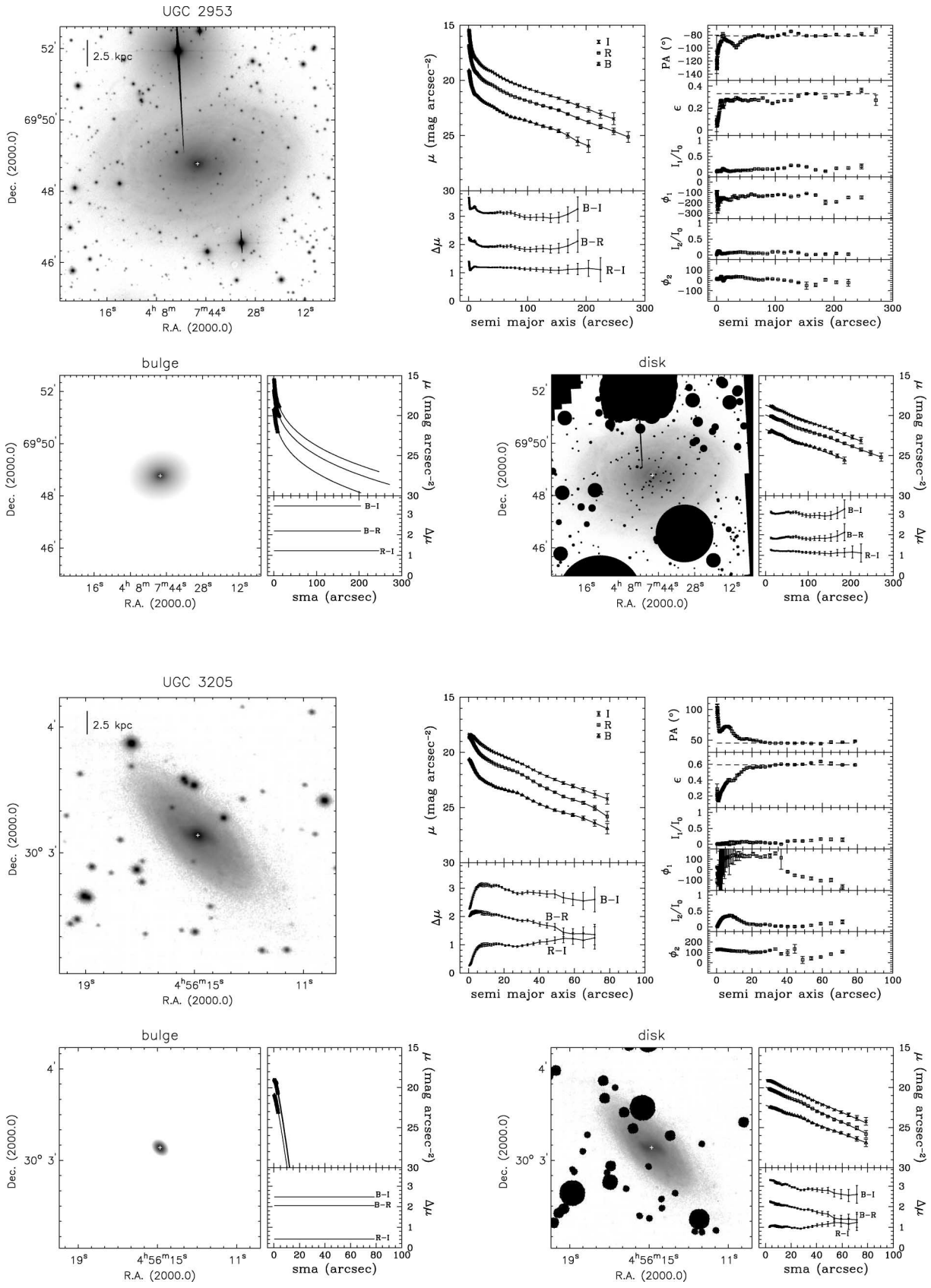

Figure B1 – *continued*

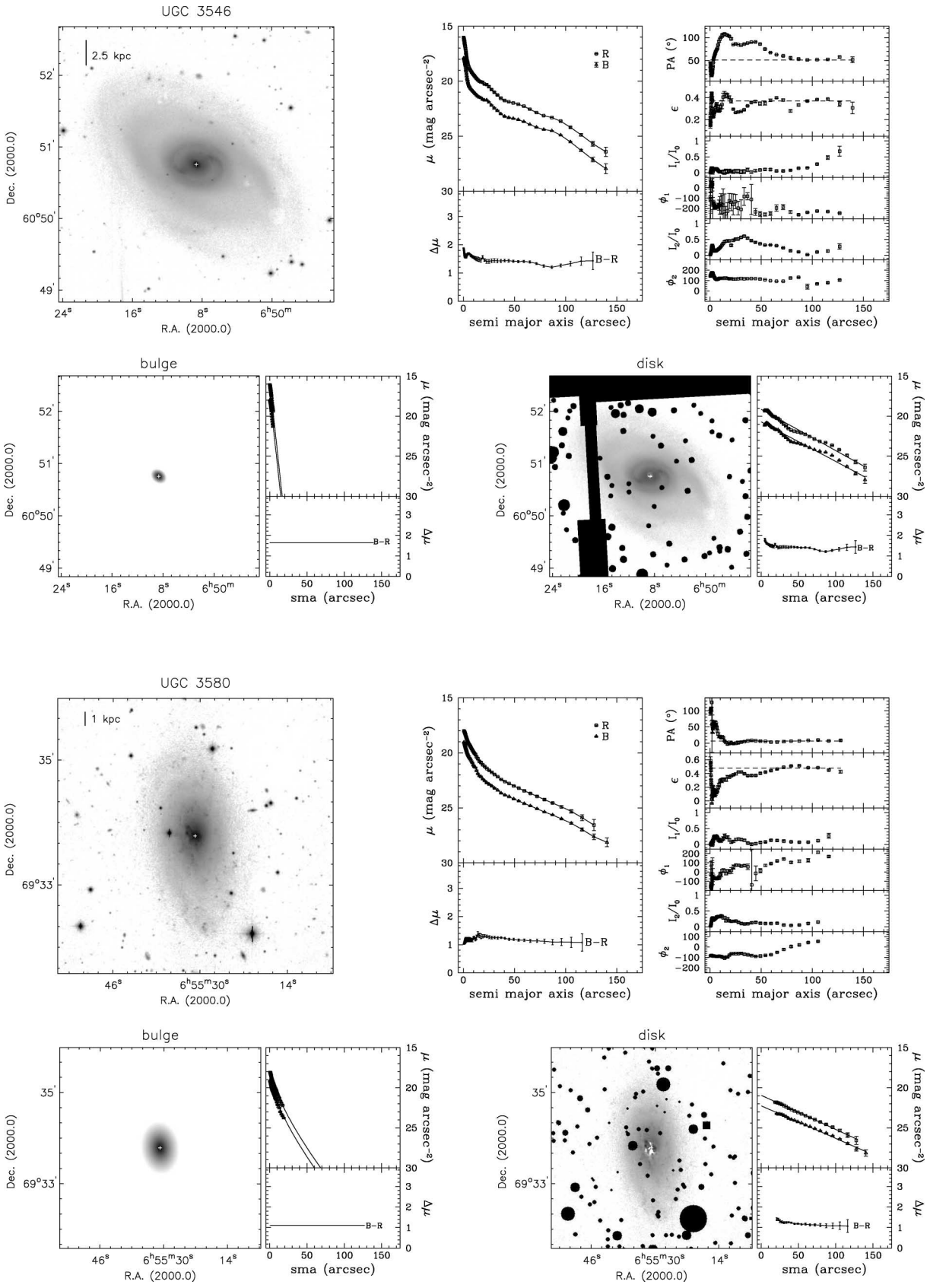

Figure B1 – *continued*

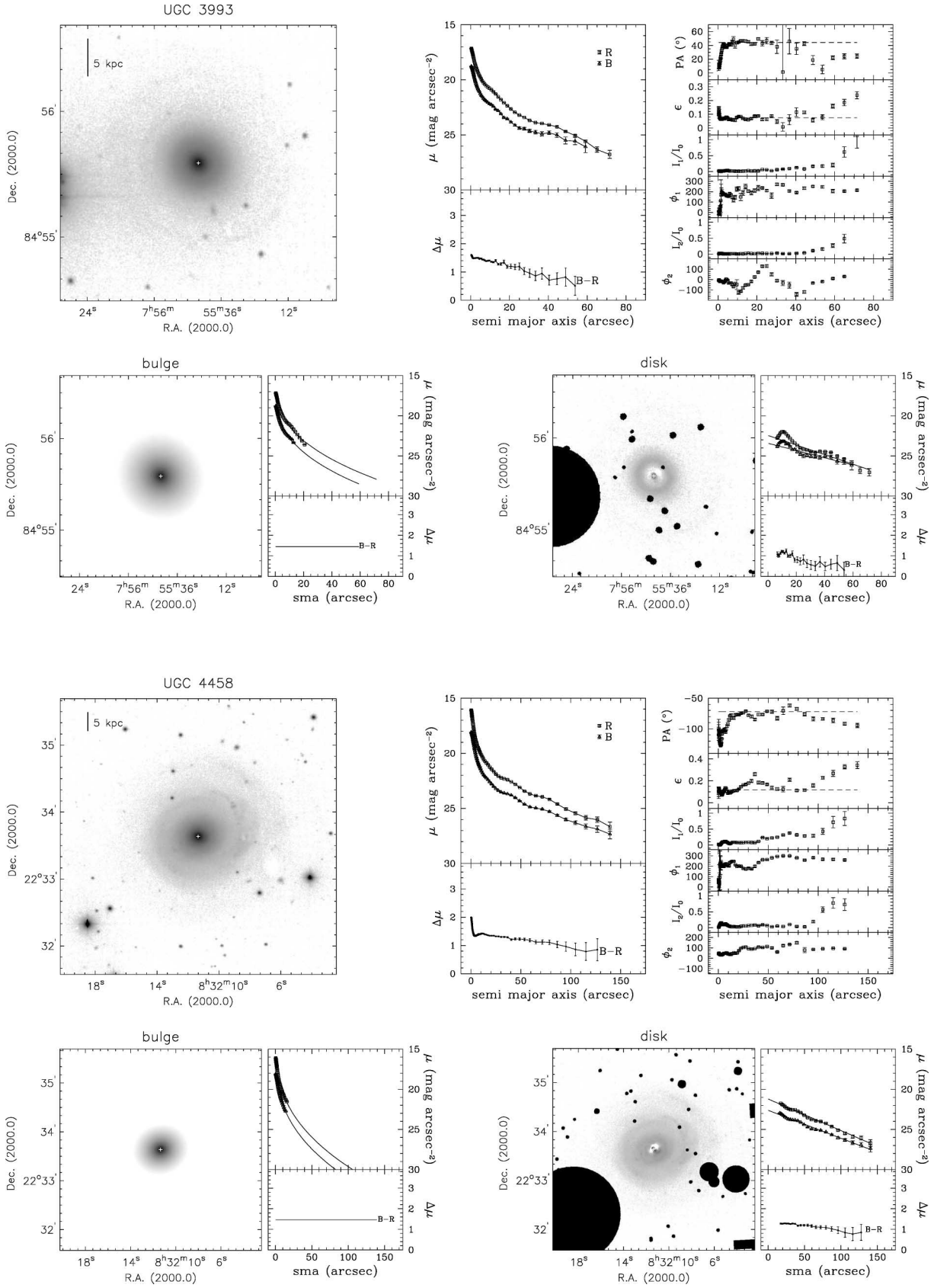

Figure B1 – *continued*

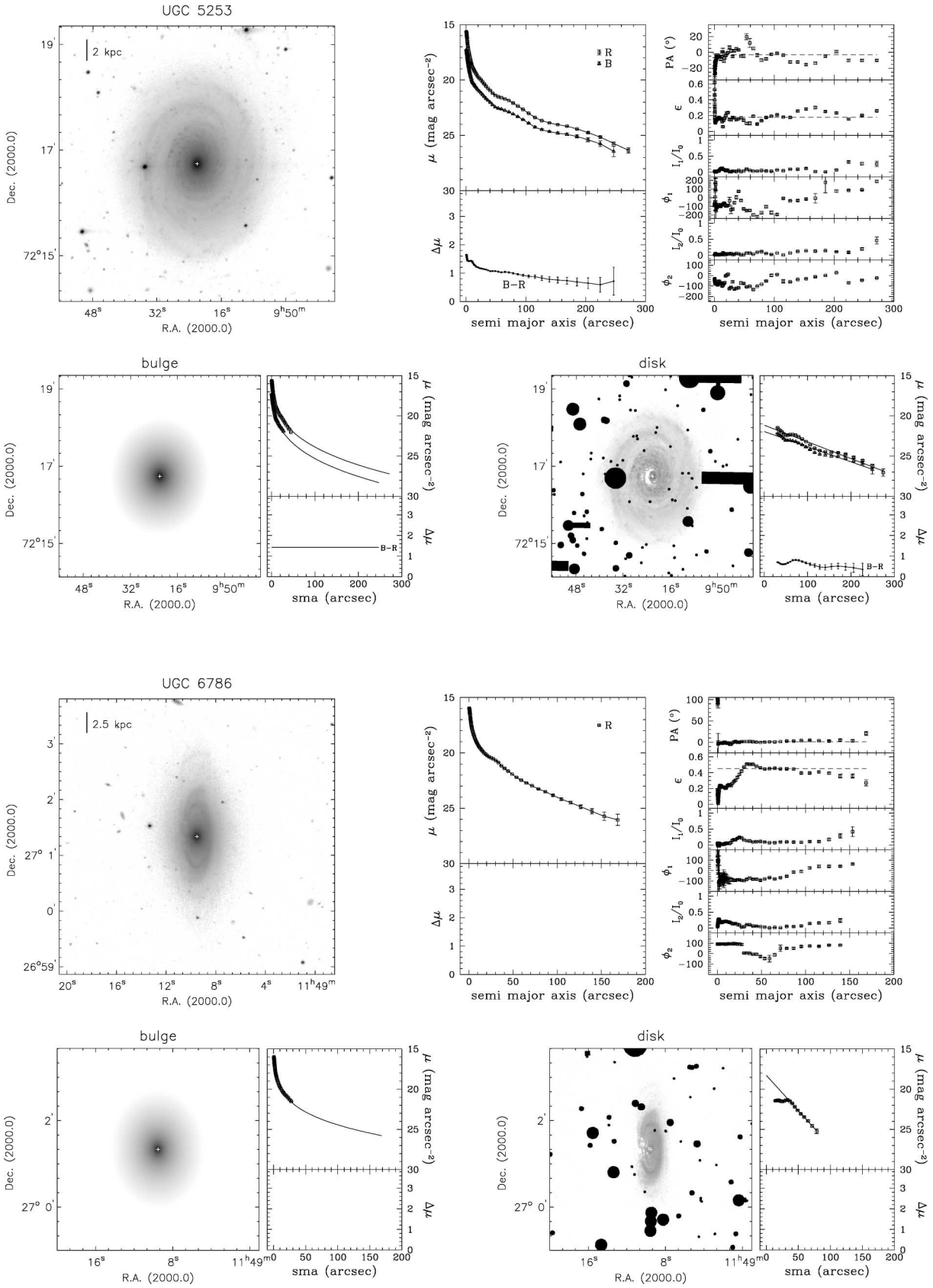

Figure B1 – *continued*

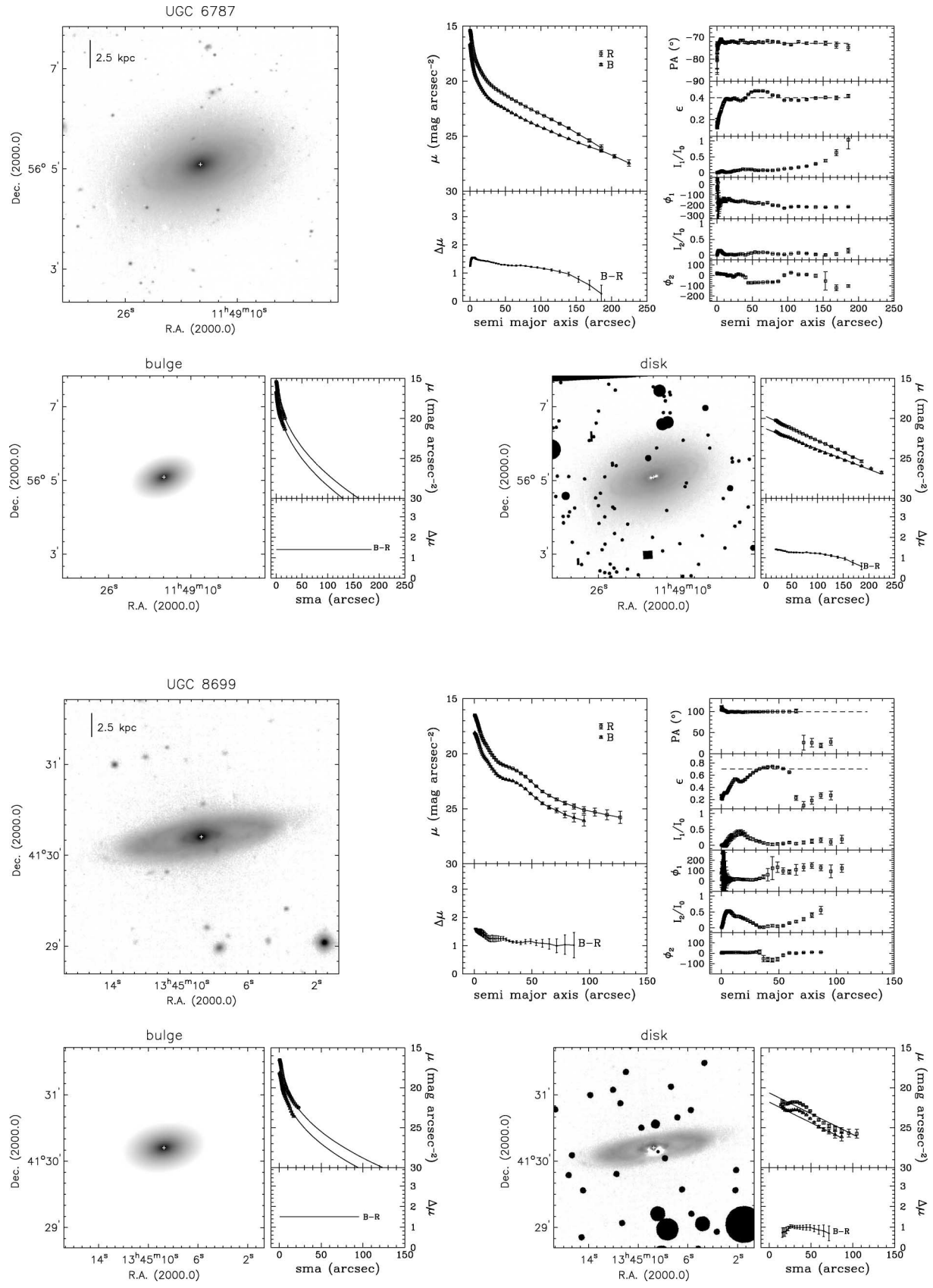

Figure B1 – *continued*

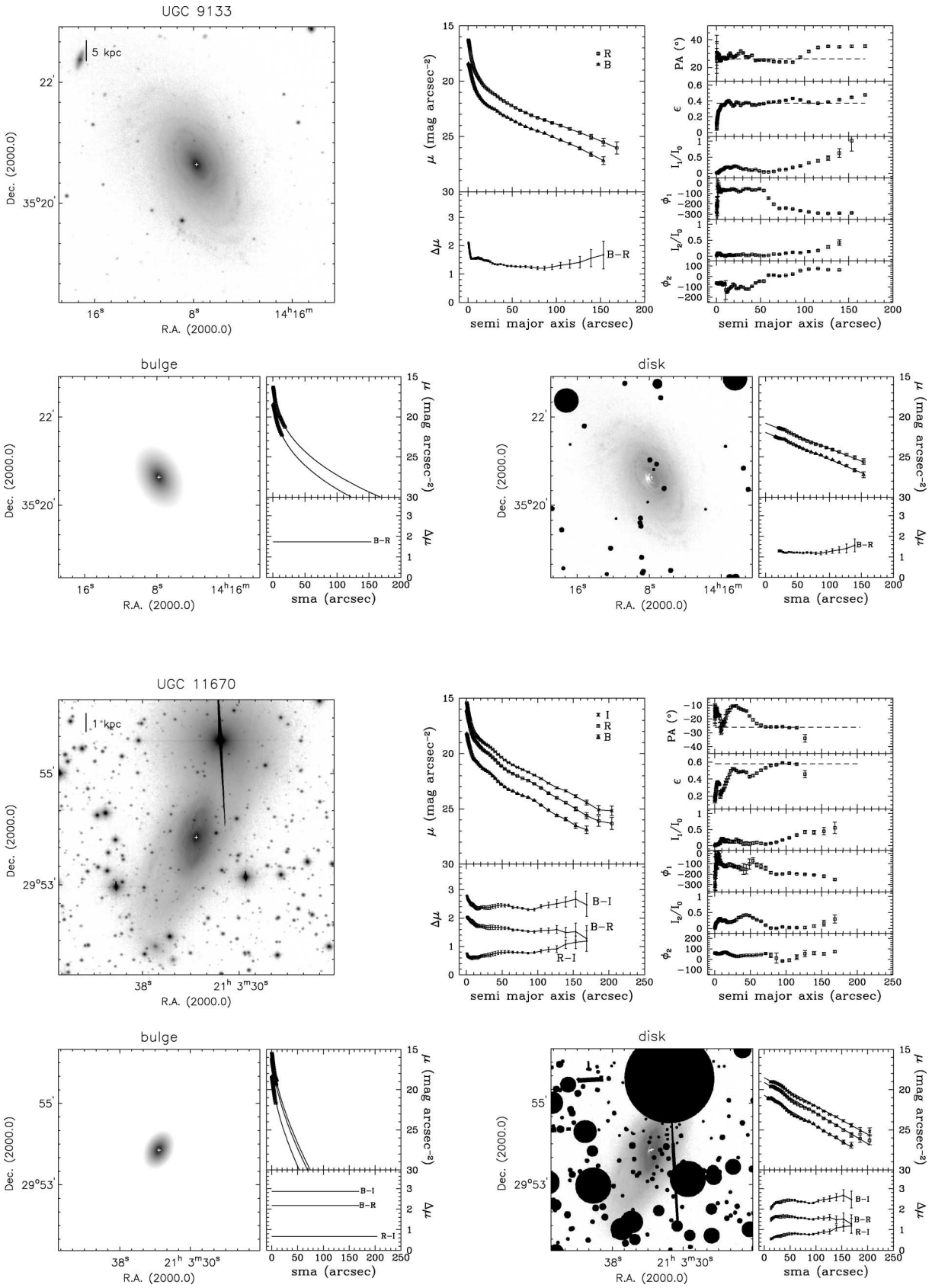

Figure B1 – *continued*

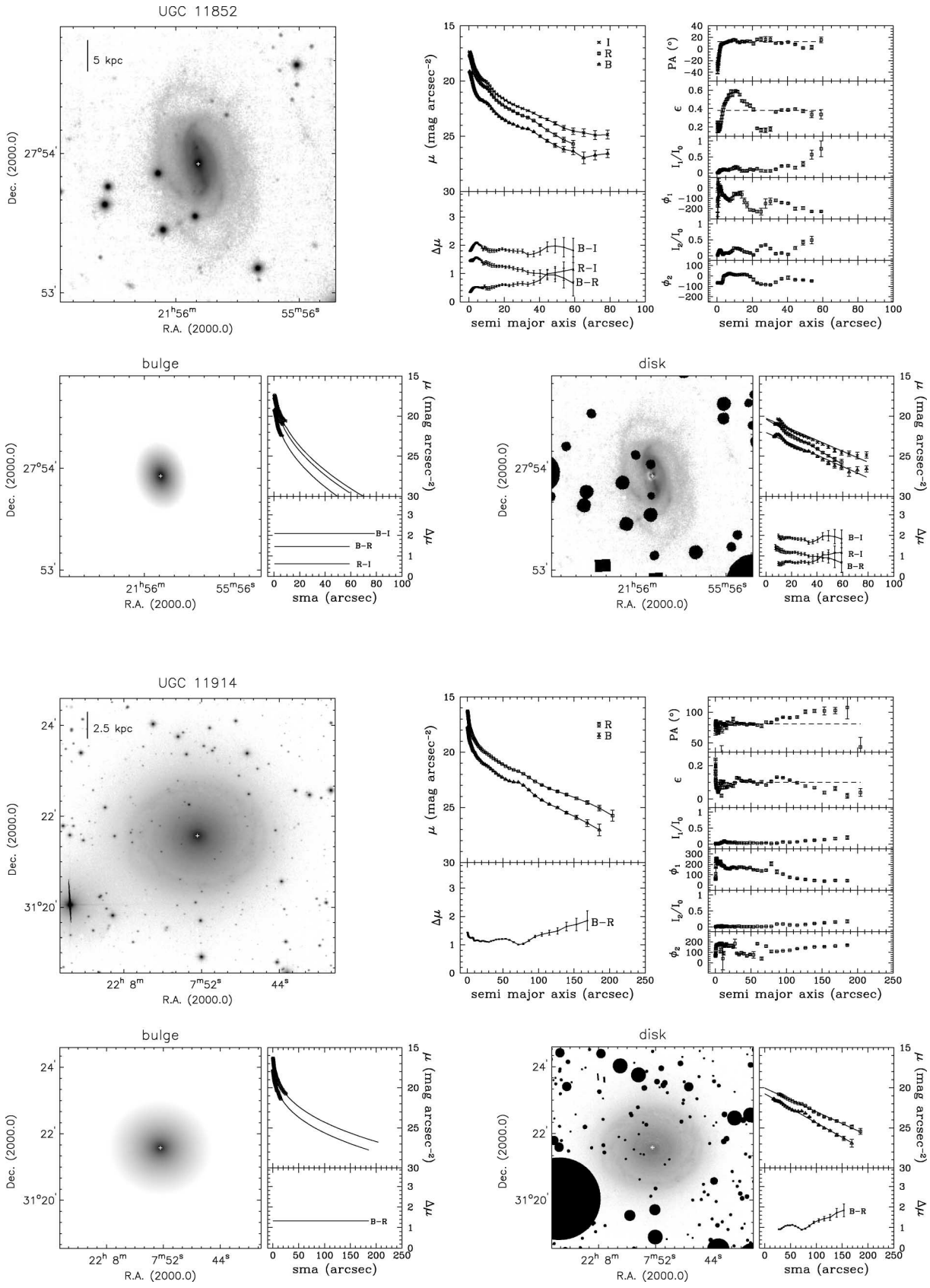

Figure B1 – *continued*

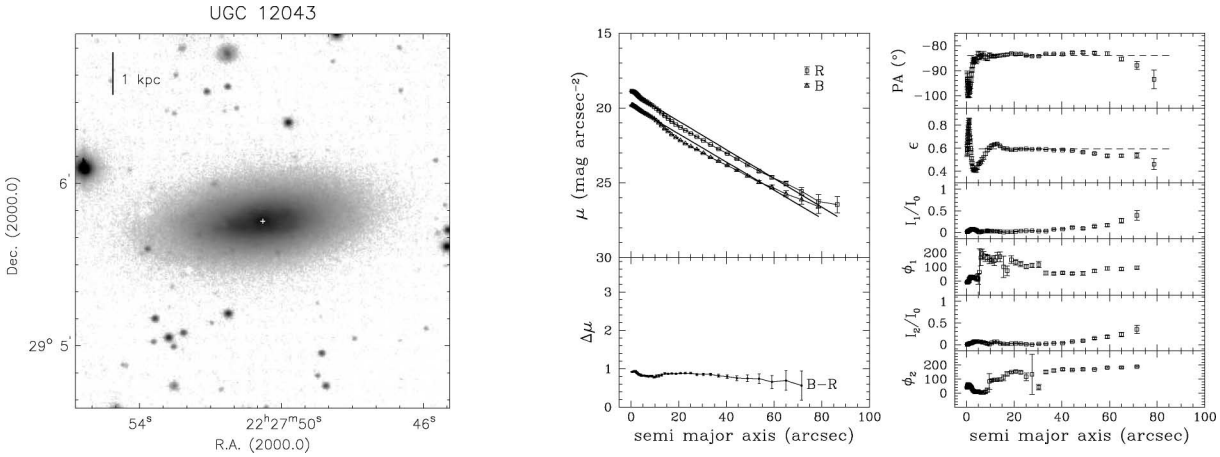

Figure B1 – *continued*

This paper has been typeset from a TEX/LATEX file prepared by the author.